Nat. Hazards Earth Syst. Sci. Discuss., https://doi.org/10.5194/nhess-2019-77
Manuscript under review for journal Nat. Hazards Earth Syst. Sci.
Discussion started: 10 April 2019

Mapping the susceptibility of syn-eruptive rain-triggered lahars at Vulcano island (Italy) combining field characterization and numerical modelling

Valérie Baumann[1], Costanza Bonadonna[1], Sabatino Cuomo[2], Mariagiovanna Moscariello[2], Sebastien Biass[3], Marco Pistolesi[4], Alessandro Gattuso[5]

[1] Department of Earth Sciences, University of Geneva, Rue des Maraîchers 13, 1205 Geneva, Switzerland

[2] Laboratory of Geotechnics, University of Salerno, Via Giovanni Paolo II 132, 84081 Fisciano Salerno, Italy

[3] Earth Observatory of Singapore, Nanyang Technological University, Singapore, Singapore

[4] Dipartimento di Scienze della Terra, Università di Pisa, Pisa, Italy

[5] Istituto Nazionale di Geofisica e Vulcanologia, Sezione Palermo, Italy

Correspondence to: Costanza Bonadonna (Costanza.Bonadonna@unige.ch)

Abstract. Lahars are a widespread phenomenon on Vulcano island (Italy), where many loose pyroclastic deposits provide a significant source of sediments. In this study we have estimated the volumes of tephra-fallout deposit that could be remobilized by rainfall-triggered lahars in association with two eruptive scenarios that have characterized the activity of La Fossa cone: a long-lasting Vulcanian cycle and a subplinian eruption. The spatial distribution and volume of tephra-fallout deposits that could potentially trigger lahars were analysed based on a combination of tephra-fallout probabilistic modelling (with TEPHRA2), slope stability modelling (with TRIGRS), field observations and geotechnical tests. Field characterization includes tephra-fallout primary deposits in the lahar initiation zones and lahar deposits both on the volcanic cone and in the ring plain. Model input data (hydraulic conductivity, friction angle, cohesion, total unit weight of the soil, saturated and residual water content) were obtained from both geotechnical tests and field measurements. In particular, hydraulic conductivity plays an important role on the stability of tephra-fallout deposits. Our parametric analysis has shown that the tephra-fallout critical thickness required to trigger a lahar for the considered rainfall event is between 20-25 cm for the Vulcanian scenario, and between 10-65cm or <10cm for a subplinian event depending on the hydraulic conductivity. The scenario remobilizing the largest unstable volumes by rain-triggered lahars is, therefore, that associated with a Vulcanian cycle with duration of 18 months and a subplinian eruption of VEI 3 (for low hydraulic conductivity). TRIGRS simulations show that shallow landsliding is an effective process for eroding the primary tephra-fallout deposits in combination with high-intensity rainfall events with short duration, such as those occurring on Vulcano every year. Our results provide a new innovative treatment of the cascading effect between tephra fallout and lahar susceptibility that also accounts for detailed characterization of source sediments based on field observations and geotechnical tests.

1 Introduction

Lahars, Indonesian term to indicate volcanic debris flows and hyper-concentrated flows with various amount of volcanic solid content, can cause loss of life and damage to infrastructure and cultivated lands and represent one of the most significant hazards for people living in volcanic areas (Pierson et al., 1990, 1992; Janda et al., 1996 ; Scott et al., 1996, 2005; Lavigne et al., 2000a; Witham, 2005; De Bélizal et al., 2013). The most destructive lahars were caused by break out of crater lakes or volcano dammed lakes (e.g., Mt. Kelud in Indonesia; Thouret et al., 1998) or by the interaction of hot pyroclastic density currents (PDCs) with glacial ice and snow at ice-capped volcanoes (e.g. Nevado del Ruiz in Colombia; Pierson et al., 1990). However, the most common lahars are those generated by heavy rainfalls on tephra fallout and pyroclastic density current (PDC) deposits emplaced on volcano slopes (e.g. Casita Volcano, Nicaragua (Scott et al., 2005); and Panabaj, Guatemala (Charbonnier et al., 2018)). For example, torrential rainstorms on loose pyroclastic deposits produced by the 1991 eruption of Pinatubo (Philippines) have generated hundreds of lahars for years after the eruption end (e.g., Janda et al., 1996; Newhall and Punongbayan, 1996). Despite their relatively small volumes, these lahars have remobilized over 6 years 2.5 km^3 of the 5.5 km^3 of primary pyroclastic material. After the 1991 eruption, during many years filling of downstream channels and overbank flows inundated villages and fields (400 km^2) and more than 50,000 people were evacuated (Vallance and Iverson, 2015).

Rain-triggered lahars may be influenced by several factors such as amount of rainfall, stratigraphy, slope gradient, vegetation cover and the physical characteristics of pyroclastic deposits (e.g., thickness, permeability, pore pressure and grain-size distribution). Rain-triggered lahars occur due to two main mechanisms: sheet and rill erosion due to Hortonian overland flow caused by deposit saturation (e.g., Collins and Dunne, 1986; Cuomo et al., 2015) and infiltration of slope surface by rainfall that can generate shallow landslides (e.g., Iverson and Lahusen, 1989; Manville et al., 2000; Crosta and Dal Negro, 2003; Zanchetta et al., 2004; Volentik et al., 2009; Cascini et al., 2010). Infiltration occurs when the rainfall intensity is lower than the hydraulic conductivity, while overland runoff occurs when rainfall intensity is greater than infiltration capacity, which is also related to capillary suction for unsaturated soils (Cuomo and Della Sala, 2013). Overland runoff is enhanced by the emplacement of very fine ash layers (< 0.125 mm) that reduces infiltration capacity (Collins and Dunne, 1986; Leavesley et al., 1989; Pierson et al., 2013; Cuomo et al., 2016). Poor infiltration capacities of fresh pyroclastic deposits have been measured at Mt. St. Helen 1980, USA (Collins and Dunne, 1986; Leavesly et al., 1989; Major et al., 2000; Major et al., 2005), Mt Uzen 1990-1995, Japan (Yamakoshi and Suwa, 2000; Yamamoto, 1984) and Chaitén 2008, Chile (Pierson et al., 2013).

The combination of a large supply of loose pyroclastic deposits and intense rainfall episodes therefore increase the likelihood of lahars. This is the case on Vulcano island (Italy; Fig. 1), where the deposits of the 1888-1890 eruption, the last eruption of La Fossa, are still remobilised during the rainy season (e.g., Frazzetta et al., 1984; Dellino and La Volpe, 1997; De Astis et al., 2013; Di Traglia et al., 2011). The initiation mechanism of recent lahars has been studied by Ferrucci et al., (2005), but the initiation mechanism during and after long-lasting eruptions and in association with short sustained eruptions (such as the eruptions that have characterized the activity of the volcano of the last 1000 years; Di Traglia et al., 2013) has not yet been characterized. Identification of lahar source areas and lahar initiation mechanisms is crucial to the evaluation of lahar recurrence and magnitude. We refer to "lahar source areas" as areas with pyroclastic material that can be remobilized to form the lahars; these areas are normally located on steep slopes (> 20°), and at the head of channels draining the volcano flanks. Based on the physical characteristics (high permeability) of the tephra-fallout deposits and on the rainfall events characteristics, we assume that the most probable rain-triggered lahar initiation mechanism on la Fossa is shallow landsliding. The later is produced by an increase of water pore pressure due to rainfall infiltration on tephra deposits which causes a slope failure. Several slope stability models have been used to predict lahar initiation processes as shallow landslides in volcanic areas (e.g. Cascini et al., 2010; Frattini et al., 2004; Crosta and Dal Negro, 2003; Cuomo and Iervolino, 2016; Cuomo and Della Sala, 2016; Cascini et al., 2011; Sorbino et al. 2007, 2010; Mead et al., 2016, Baumann et al., 2018). Among those, the model TRIGRS (Baum et al., 2002) can be used for computing transient pore pressure and the related changes in the factor of safety due to rainfall infiltration. Here, TRIGRS is used to investigate the timing and location of shallow landslides in response to rainfall in large areas (e.g. Baumann et al., 2018).

Lahars represent a complex hazard volcanic phenomenon strongly related to the availability and characteristics of the source pyroclastic material (e.g. tephra, PDC), geological and geomorphological characteristics of the area and climatic conditions (mostly precipitation). Tierz et al. (2017) have already show the importance of assessing the effect of cascading hazards by compiling a probabilistic lahar hazard assessment through the Bayesan belief network "Multihaz" based on a combination of probabilistic hazard assessment of both tephra fallout and PDCs and a dynamic physical model for lahar propagation. Nonetheless, the use of physically-based models for the determination of deposit instability in combination with field observations is also necessary for an accurate characterization of the lahar triggering process. Our goal is to accurately predict the volume of tephra fallout that could be remobilized by a rainfall-triggered shallow landslide in association with various eruptive conditions at La Fossa cone in order to compile a rain-triggered lahar susceptibility map. To achieve this task, we combine the shallow landslide model TRIGRS with both probabilistic modelling of tephra fallout (for eruptions of different time and magnitude) and field and geotechnical characterisations of tephra-fallout deposits (i.e. grainsize, hydraulic conductivity, soil suction, deposit density).

First, we describe the physical characteristics (e.g., grainsize, hydraulic conductivity, angle of friction) of selected tephra-fallout deposits associated with both a long-lasting Vulcanian eruption (i.e., the 1888-90 eruption) and a subplinian eruption (Pal D eruption of the Palizzi sequence; Di Traglia et al., 2013). For clarity, we refer to the deposits of the last 1888-1890 long-lasting Vulcanian event as the "1888-90 eruption" and to the fallout deposit of the subplinian Palizzi D eruption as "Pal D" primary deposits. Second, we characterize lahar deposits associated with the 1888-90 eruption, which provide insights in source areas, flow emplacement mechanisms and inundation areas of future lahars. The tephra-fallout deposits characteristics are used in combination with a probabilistic modelling of tephra fallout (Biass et al., 2016) to estimate the unstable areas based on the shallow landslide model TRIGRS (Baum et al., 2002). This approach provides the first integrated attempt to quantify the source volume of lahars as a function of probabilistic hazard assessment for tephra fallout (with TEPHRA2), numerical modelling of lahar triggering (with TRIGRS), field observations (including primary tephra-fallout deposits, geology, geomorphology and precipitations), and geotechnical tests of source deposits. Finally, we propose a new strategy to map the syn-eruption lahar susceptibility as a critical tephra thickness resulting in unstable conditions, which could represent a valuable tool for contingency plans. Here the term syn-eruptive is used in the sense of Sulpizio et al. (2006) to indicate lahars originated during volcanic eruptions or shortly after, while post-eruptive lahar events are generated long (i.e. few to several years) after an eruption. To sum up, this study explores the problematic of volcanic multi-hazard assessment and offers an innovative treatment of the cascading effects between tephra fallout and lahar susceptibility.

2 Study area

2.1 Eruptive history

The island of Vulcano, the southernmost island of the Aeolian archipelago, consists of several volcanic edifices whose formation overlapped in time and space beginning 120 ka ago **(Fig. 1)**. The most recently active volcano is the La Fossa cone, a 391 m-high active composite cone that began to erupt 5.5 ka ago (Frazzetta et al., 1984). Historical chronicles (Mercalli and Silvestri, 1891; De Fiore, 1922), archeomagnetic data (Arrighi et al., 2006; Zanella et al., 1999; Lanza and Zanella, 2003) and stratigraphic investigations (Di Traglia 2013; De Astis et al. 1997, 2013) indicate that in the past 1000 years at least 15 effusive and explosive eruptions have occurred. This period of eruptive activity has been recently divided into two main eruptive clusters. The eruptive activity of Palizzi and Commenda units is grouped into a single eruptive period (Palizzi-Commenda Eruptive Cluster), lasting approximately 100 years during the 13th century. The younger Pietre Cotte cycle, the post-1739 AD and the 1888–1890 AD activity form the Gran Cratere eruptive cluster (1444-1890 AD; Di Traglia et al., 2013). The composition of the products erupted at La Fossa varies from latitic to rhyolitic, with minor shoshonites (Keller, 1980; De Astis et al., 1997; Gioncada et al., 2003). In this work, we will focus on the tephra fallout associated with two main eruptive styles of the past 1000 years: subplinian eruption, which emplaced deposits such as the the Palizzi D sub-unit, and long-lasting Vulcanian eruption such as that of 1888-90 (e.g., Di Traglia et al., 2013, Biass et al., 2016).

2.2 Climate

Vulcano island has a typical semi-arid Mediterranean climate (De Martonne, 1926) with annual rainfall between 326 mm and 505 mm, falling mostly during autumn and winter seasons **(Fig. 2a)**. Based on Arnone et al. (2013) rainfall trends in Sicily island can be classified in three intensity-based categories: light precipitation (0.1-4 mm d^{-1}), moderate precipitation (4-20 mm d^{-1}) and heavy–torrential precipitation (>20 mm d^{-1}). Events more intense than 20 mm/d occurred three times in 2010 and 2011, two times in 2012 and one time in 2013 and 2014 (INGV Palermo). The rainfall duration for the 20 mm d^{-1} events can last 2 or 3 hours to 3 days and occur normally in September, October, November and December, but can also occur in May **(Fig. 2b)**. These meteorological conditions associated with poor vegetation coverage (Valentine et al., 1998), steep slopes **(Fig. 1b)** and the presence of layered, fine-grained tephra (lapilli and ash), favour the remobilization of volcanic deposits (Ferrucci et al., 2005; Di Traglia, 2011). Wind patterns inferred from the ECMWF ERA-Interim dataset (Dee et al., 2011) for the period 1980-2010 show a preferential dispersal towards SE at altitudes lower than 10 km a.s.l., which above shift towards E (Biass et al., 2016).

2.3 Recent lahars

Both syn-eruptive and post-eruptive lahar events induced the progressive erosion of the tephra deposits which covers La Fossa cone. The tephra fallout deposit associated with the most recent Vulcanian eruption (1888-90) has been almost completely removed from the upper slopes and accumulated at the foot of the cone, where the stratigraphic sections show a succession of lahar deposits with thicknesses between 0.1 and 1 m (Ferrucci et al., 2005). All the tephra sequence of the Gran Cratere eruptive cluster (including the last 1888-90 Vulcanian eruption) lies on top of thinly stratified reddish, impermeable ash layers (Varicolored Tuffs or "Tufi Varicolori"; Frazzetta et al., 1983; Capaccioni and Coniglio, 1995; Dellino et al., 2011) which concluded the Breccia di Commenda phase. In most parts of the cone, the dark-gray tephra of the Vulcanian cycles is almost completely eroded and the “Tufi Varicolori” tuffs are exposed. A rill network developed on the impermeable fine grained tuffs that conveys water to a funnel shape area, where a main gully initiates, defines a drainage basin (Ferrucci et al., 2005). The main gullies start where the loose grey coloured interdigitated tephra fallout and lahar deposits crop out **(Fig. 1)**. Lahar volumes and travel distance strongly depend on both the availability of pyroclastic material in the source area and on the characteristics of the rainfall events (intensity and duration). Ferrucci et al. (2005) estimated volumes between 20 and 50 m^3 for 3 recent lahars based on levees and terminal lobe deposits geometry on the NW sector of La Fossa cone. However, the occurrence of larger syn-eruptive lahars (10^3-10^4 m^3) reaching the Porto di Levante and Porto di Ponente areas have been also reported (Di Traglia et al., 2013). Much of the material of the La Fossa ring plain has been transported by lahars during the post-1000 AD period; in fact, the Porto di Levante and Porto di Ponente plains were progressively filled up with 2-3 m of reworked tephra deposits during this time interval (Di Traglia et al., 2013). Di Traglia et al. (2013) also reported post-eruptive lahar deposits on the flank of the volcano with increasing thickness towards the base. Deposit thickness then decreases on the ring plain in Porto area where they also show finer grainsize and lamination.

The study of recent lahars located on the NW flank of La Fossa cone indicated that the deposits were emplaced by saturated slurries in which grain interaction dominated the flow dynamics (Ferrucci et al., 2005). The use of empirical ratio clay/(sand+silt+clay) (Vallance and Scott, 1997) and the physically based calculation of Nmass (Iverson and Vallance, 2001) suggest non-cohesive debris flows and transport dominated by granular flows (Ferrucci et al., 2005).

3 Methods

3.1 Field sampling

The field characterization of both fallout primary deposits in the lahar initiation zones and lahar deposits was carried out during two field campaigns in 2017 and 2018. A total of eight samples were collected from undisturbed outcrops on the La

Fossa cone and Palizzi valley for the 1888-90 and the Pal D primary deposits (Fig. 1) in order to retain primary physical characteristics. Besides 11 samples were collected from the 1888-90 and Pal D primary deposits sections for grain-size analysis (Fig. 3). For the 1888-90 deposit, four samples were collected in the lahar initiation zone on the S flank of La Fossa cone, where the deposit crops out in the inter-channel zone (V1 in Fig. 1). On the NW flank of La Fossa, since most of the 1888-90 primary deposit is covered with remobilized material, two samples were taken from outcrops in the upper part of the cone where the minimum disturbance occurred (V2 in Fig. 1). Two samples of the Pal D primary deposit were collected in the Palizzi valley (V3 and V4 in Fig. 1). Note that the lahar source area associated with the Pal D primary deposit is either covered by the new eruptive products or eroded. We chose the two most complete sections and dug the most recent products.

Deposit sampling was performed by inserting a steel tube with a height of 30 cm and a diameter of 10 cm into the ground (see Appendix A, Fig A1). A basal support was then inserted, and the tube extracted from the deposit with a minimum disturbance of the internal stratigraphy. The tube was then covered on both ends to preserve the deposit for further laboratory analysis (see Section 3.2). Due to the sampling apparatus, only the top 30 cm of the deposits were sampled both for grainsize analysis and geotechnical tests, and our results therefore do not provide a comprehensive characterization of the whole deposit. Despite this, we consider 30 cm of sampling as representative for the main characteristics of both the 1888-90 (which is thinly laminated across the entire section) and the Pal D (which is mostly massive) deposits. Soil suction measurements were carried out in situ on the 1888-90 tephra-fallout deposit with a soil moisture probe ("Quick Draw" Model 2900FI) (Fig. 1) (see Appendix A, Fig A2). The saturated hydraulic conductivity was estimated in the field with a single-ring permeameter for both deposits (see Appendix A, Fig. A3).

The field description and sampling of both syn-eruptive lahar deposits associated with the 1888-90 eruption were performed on the NW volcano flanks, in the Palizzi valley and in the Porto plain (Fig. 1). We described also a recent lahar deposit occurred in September 2017 on the La Fossa cone NW flank. Lahar matrix samples from these lahars were collected on the volcano flanks and ring plain for grainsize analyses.

3.2 Laboratory analyses

Grainsize analyses were carried out at the University of Geneva for three tephra-fallout sections (11 samples) and for 11 lahar-deposit matrix samples (fractions between -6 and 10 φ). The phi (φ) scale is a sediment particle size scale diameter calculated as the negative logarithm to the base 2 of the particle diameter (in millimeters) (Krumbein, 1938). Samples were mechanically dry-sieved at half-φ intervals for the coarser fraction between 16 mm and 0.25 mm. The laser granulometry technique (CILAS 1180 instrument) was used for fractions smaller than 0.25 mm. Deposit density of five samples of the 1888-90 primary deposits and for one samples of the Pal D primary deposit were also determined at the University of Geneva weighing a given volume of sample material measured with a graduated cylinder.

Natural water content and shear strength were measured on undisturbed samples at the University of Salerno. The natural water content (w_n) was evaluated at several depths (from 0.06 m to 0.3 m) for six samples of the 1888-90 primary deposits and for four samples of the Pal D primary deposit. The shear strength of primary deposits was measured through direct shear tests performed in conventional direct shear apparatus in the Laboratory of Geotechnics at University of Salerno. Tests on undisturbed specimens of 1888-90 primary deposit were performed at both natural water content and in fully saturated condition. The natural water content (w_n) and the degree of saturation were evaluated before and after the tests. The modified Kovacs model of Aubertin et al. (2003) was used to obtain the Soil Water Retention Curve (SWRC) from the grain size data (i.e., D_{10} and D_{60}), and the liquid limit. SWRC relates the water content to soil suction. The tests were interpreted in terms of shear stress and the vertical effective stress as defined by Bishop (1959), referring to the "effective saturation degree" (S_{re}) following Eq. (1):

$$\sigma'_{ij} = \sigma_{ij} - u_a\delta_{ij} + S_r(u_a - u_w)\delta_{ij}, \tag{1}$$

where σ_{ij} (kPa) is the total stress tensor, u_a (kPa) is the pore air pressure, u_w (kPa) is the pore water pressure, u_a - u_w is the matric suction and S_r (%) is the degree of saturation.

The saturated hydraulic conductivity $K_{s,}$ **(**m s^{-1}) for the 1888-90 primary deposit was measured through laboratory tests at the University of Salerno. The test was carried out on a reconstructed specimen with height of 140 mm and diameter of 39.4 mm obtained through water pluviation technique, ensuring specimen saturation. A constant water volume (5 ml) was forced to go through the specimens by applying a difference of pore pressure between top and bottom, while the time was measured. The test was repeated 5 times and each time K_s was evaluated.

The saturated soil diffusivity D_0 (m^2 s^{-1}) was evaluated for both deposits using the soil water retention relationship of Rossi et al. (2013) as a function of the saturated hydraulic conductivity and the parameters (h_b, λ) of Brooks and Corey (1962, 1964) following Eq. (2):

$$D_0 = \frac{h_b k_{sat}}{\lambda(100 \cdot n - \theta_s)}, \tag{2}$$

where θ_s (%) is the soil water content at the saturation, h_b (kPa) the bubbling pressure and λ (m^2 g^{-1}) the pore size index distribution. The parameters h_b and λ were estimated interpolating the data of SWRC.

3.3 Probabilistic tephra modelling

In order to best describe the cascading effect between tephra deposition and lahar triggering susceptibility in a context of multi-hazard assessments, tephra deposits considered in our analysis are those probabilistically modelled by Biass et al. (2016). Based on the stratigraphy of the last 1000 years of La Fossa (Di Traglia et al., 2013), Biass et al. (2016) defined three eruption scenarios for tephra fallout including: i) a long-lasting Vulcanian eruption scenario (plume heights: 1-10 km a.s.l.; total mass: 1.9-140 × 10^9 kg; duration: 30 days-3 years); ii) a VEI 2 (Volcanic Explosivity Index, Newhall and Self, 1982) subplinian eruption scenario (plume heights: 5-12 km a.s.l.; mass: 0.6-6 ×10^9 kg; duration: 0.5-6 h); and iii) a VEI 3 subplinian eruption scenario (plume heights: 8-17 km a.s.l.; mass: 6-60× 10^9 kg; duration: 0.5-6 h). Note that although no VEI 3 eruption is observed in the stratigraphy of the last 1000 years of activity, evidences of VEI 3 eruptions are found in the older history of La Fossa. All three scenarios were simulated probabilistically using the Tephra2 model (Bonadonna et al.,

2005) through the TephraProb software (Biass et al., 2016b).

Probabilistic isomass maps were computed for various probability thresholds, which express the distribution of tephra load for a fixed probability of occurrence within a given eruption scenario (Biass et al., 2016b). For the long-lasting Vulcanian scenario, various probabilistic isomass maps were computed to express the cumulative tephra fallout at a given time after eruption onset. Note that these cumulative maps ignore remobilization of the primary deposit between single Vulcanian explosions. These isomass maps were converted to isopach maps using deposit densities of 1200 kg m^{-3} and 600 kg m^{-3} for the Vulcanian and subplinian scenarios, respectively (Biass et al., 2016).

3.4 TRIGRS model

The Fortran Program TRIGRS of Baum et al. (2002) computes transient pore pressure changes and related changes in the safety factors due to rainfall infiltration. Baum et al. (2002) extended the method of Iverson (2000) by implementing the solutions for complex time sequence of rainfall intensity, an impermeable basal boundary at infinite depth and optional unsaturated zone above the water table. The reader is referred to the vast literature published on the application of this model for more details (e.g., Baum et al. 2002, 2008, Savage et al., 2003; Salciarini et al., 2006, Cuomo and Iervolino, 2016). Briefly, the infiltration models in TRIGRS for wet initial conditions are based on Iverson's (2000) linearized solution of the Richards equation and its extention to that solution (Baum et al., 2002; Savage et al., 2003, 2004). The solution is valid only where the transient infiltration is vertically downward and the transient lateral flow is relatively small.

The model computes the transient pore pressure and changes in the safety factor at different depth due to rainfall infiltration. In addition, TRIGRS model is applicable for unsaturated initial conditions, with a two-layers system consisting of a saturated zone with a capillary fringe above the water table overlain by an unsaturated zone that extends to the ground surface. The unsaturated zone acts like a filter that smoothes and delays the surface infiltration signal at depth. The model uses the soil-water characteristic curve for wetting of the unsaturated soil proposed by Gardner (1958) and approximates the infiltration process as a one-dimensional vertical flow (Srivastava and Yeh, 1991, Savage et al., 2004).

Following Iverson (2000), slope stability is calculated using an infinite-slope stability analysis. Incipient failure of infinite slopes is decribed by an equation that balances the downslope component of gravitational driving stress against the resisting stress due to basal Coulomb soil friction and the influence of groundwater (Iverson, 2000). The Factor of Safety (FS) is calculated at a depth Z by Eq. (3):

$$FS\,(Z,t) = \frac{tan\phi'}{tan\beta} + \frac{c' - \psi\,(Z,t)\gamma_w tan\phi'}{\gamma_s Z sin\beta cos\beta} \qquad (3)$$

where c' (kPa) is the effective soil cohesion, ϕ' (deg) is the effective friction angle, $\psi(Z,t)$ is the ground water pressure head ψ (kPa) as a function of depth Z (m) and time t (s), β (deg) is the slope angle, Υ_w (kN m^{-3}) is the unit weight of groundwater and Υ_s (kN m^{-3}) is the unit weight of soil. The pressure head ψ (Z, t) in (3) is obtained from various formula depending on the

Nat. Hazards Earth Syst. Sci. Discuss., https://doi.org/10.5194/nhess-2019-77
Manuscript under review for journal Nat. Hazards Earth Syst. Sci.
Discussion started: 10 April 2019

particular condition modelled.

FS is calculated for pressure heads at multiple depths (*Z*). The slope is predicted to be instable where FS< 1, in a state of limiting equilibrium where FS=1 and stable where FS>1. Thus, the depth *Z* of landslide initiation is where FS first drops below 1.

The TRIGRS model for unsaturated initial conditions was applied on the probabilistic isopach maps described in section 3.3 for the long-lasting Vulcanian, the subplinian VEI2 and the subplinian VEI3 eruption scenarios. For each eruption scenario, probabilistic isopach maps are computed for probabilities of occurrence of 25% and 75% (Biass et al., 2016). The eruption associated with the subplinian scenario is considered to be short lived (<6 hours), and therefore, one single deposit is analysed. Instead, for the long-lasting Vulcanian scenario, deposits are computed for durations of 3, 6, 9, 12, 18 and 24 months.

A 5-m resolution Digital Elevation Model (DEM) of Vulcano Island was used in our susceptibility analysis that was computed from contour lines and spots heights reconstructed from stereo-photograms at a scale of 1:35000 collected during an aerophotogrametric flight in 1994-5 (Bisson et al., 2003). The maximum planimetric error of the contour lines reconstructed from stereo models is less than 3.5 m. The vertical error of the DEM is lower than 0.5 m in the area of La Fossa cone and <1 m in the flat area of Vulcano Porto (Bisson et al., 2003).

4 Results

4.1 Field characterization of tephra and lahar deposits

Pal D deposit

We logged two sections of the Pal D primary deposit at outcrops located in the Palizzi Valley (point V3 and V4, Fig. 1). The isopach map (Di Traglia, 2011) in Fig. 1b show the southward dispersal of Pal D primary deposit distribution on Vulcano island. The section is a 1 m-thick, massive, grain supported and well-sorted pumice deposit (Fig. 3 A). The Pal D deposit occurs between two sub-units of the Palizzi cycle. At the base, Pal C deposit (alternation of black lapilli and ash) crops out, while on top of Pal D the rhyolitic white ash of Rocche Rosse eruption from Lipari and the Breccia di Commenda are present (Di Traglia et al., 2011; Rosi et al., 2018). The mean saturated hydraulic conductivity of the Pal D deposit measured in the field is 6.8×10^{-4} m s^{-1} (Table 1).

1888-90 deposit

Two stratigraphic sections of the 1888-90 primary deposit were logged in the upper part of the La Fossa cone S flank (V1; Fig. 3 C) and at the base of the NW flank (V2; Fig. 3 D). The isopach map for 1888-90 primary deposit shows its almost circular dispersal (Fig. 1 c). The V1 section overlies several older tephra fallout and lahar units (Fig. 1). It is a 1 m-thick deposit consisting of an alternation of thin ash and lapilli layers overtopped by 0.2 m of reworked tephra. The whole sequence shows an inclination of 30°. The second section (V2) is a 0.5 m-thick deposit laying on the Commenda tephra sequence and is overlaid by 0.3 m of reworked tephra. Seven soil suction measurements on the 1888-90 deposits located on the La Fossa cone in the upper catchment and lower part of the cone (Fig. 1) are comprised between 15 kPa and 27 kPa (Table 2). The mean saturated hydraulic conductivity measured in the field varies between 6.0 and 7.5 × 10^{-5} m s^{-1} (Table 1).

Syn-eruptive lahars (1888-90 eruption)

Here, we use *syn-eruptive* lahars to describe events that occurred during and shortly after the 1888-1990 eruption cycle. Stratigraphic sections in gullies and small channels on the NW flank of the la Fossa cone show several massive to laminated, remobilized deposits covering the 1888-90 primary tephra. Assessing the areal distribution and the correlation between different lahar deposits is difficult since no lahar map on Vulcano exist. The thickness of each lahar layer, representing different flow pulses, varies between ~ 0.20 and 1 m. The lahars are massive to thinly laminated, matrix-supported deposit, with boulders immersed in a coarse ash and lapilli matrix. The observed boulders have diameter between 5 and 15 cm. Although the distinction among debris flow and hyperconcentrated flow emplacement mechanisms from the direct observation in the field was not possible due to the lack of information related to original water content, we speculate that most of the well-sorted, massive deposits were related to hyperconcentrated flows based on the definition of Pierson (2005). 11 samples (total number) of lahar matrices were sampled on the S cone flank (V5; Fig. 4a), on the NW cone flank (V8-V10; Fig 4d), in the Palizzi valley (V6; Fig 4b) and in the Porto Plain (V7-1-4; Fig. 4f), where the matrices of four lahars were sampled from distinctive episodes.

September 2017 lahar

We also described a small lahar event that occurred in September 2017, one month before our 2017 field work (Fig. 4e). The lahar source area was located on the NW cone flank in a funnel shaped area located above a small gully at an elevation of 159 m a.s.l. The lahar flowed into a gully with an average width of 2 meter and a depth varying between 0.4 and 0.8 m, formed levees on both sides and stopped on the La Fossa crater trail with a final runout of 120 m. The area of the front lobe deposit was measured with a handheld GPS (135.5 m^2) and approximate thickness estimated (0.3 m) in the field, which resulted in a volume of ~40 m^3. A second lahar flow pulse deposited a small deposit confined within the channel (Fig. 5e). Two samples (V11 and V12) were taken from this recent lahar deposit in order to compare with the older syn-eruptive lahar deposits.

4.2 Laboratory characterization of tephra and lahar deposits

Grain-size analyses

Grain-size distributions of all samples are summarized in Table 3 and Figure 5. The Mdϕ of the majority of samples is in the range of 2ϕ and -1ϕ and most deposits are well sorted. Grain-size distribution of primary deposits are presented in Figure 6a. The grain-size distribution of the top 30 cm of the Pal D primary deposit at section V3 shows Mdϕ and σϕ of -3.42 and 1.55, respectively (Table 3). Grain-size distributions of the top 30 cm of the 1888-90 primary deposit on the S flank of La Fossa

(V1) show Mdϕ of -0.88–0.08 and σϕ of 1.46–1.80, respectively (Table 3). At the base of the cone on the NW sector (V2), grain-size distributions are slightly finer (Mdϕ of 0.09 to 0.9) and with a poorer sorting (σϕ of 1.49 to 2.1). Generally, the grain-size distributions of the top 30 cm of sections V1 and V2 show a predominance of coarse ash (Fig. 3) but V2, located at the base of the cone, contains more fine ash. Grain-size distribution of lahar matrices are presented in Figure 6b. All matrix samples have a low content of fine ash (i.e., 2.4–16%). The matrix is composed primarily of 60–83% coarse ash and 2–36% of lapilli. The Mdϕ vs σφ diagram shows a finer grain-size distribution for lahar matrices located in the Palizzi valley and Porto di Ponente harbour (V6 and V7 samples, respectively, Fig. 5) than for those located on the La Fossa cone (V5 sample, Fig. 5). The grain-size distribution for older (V8–10 samples, Fig. 5) and more recent (V11–12 samples, Fig. 5) lahars are in the same range. In general, the grain-size distributions of the 1888-90 primary deposits is similar to their remobilized counterparts (Figs. 5, 6; Table 3). Only three primary deposits are coarser than lahar matrices (V1C, V1D and V3; Fig. 5)

Natural water content

The natural water content (w_n) of the 1888-90 primary deposit varies from 2.64% to 3.65%, while Pal D primary deposit exhibit higher w_n (10.80–30.63%). The specific gravity (G_s) for the solid fraction was measured for both deposits and shows values of 2.57 and 2.42 for the 1888-90 and Pal D primary deposits, respectively.

Shear strength

Although the four specimens of 1888-90 primary deposit are consolidated at three different total stresses, all specimens exhibit a slight hardening associated to a dilative behaviour. The shear stress envelope exhibit high friction angle ($\phi = 42°$) and nil cohesion (Table 4). For Pal D primary deposits, direct shear tests are performed on reconstructed specimens constituted only by sandy fraction, smaller than 20 mm. The specimen is reconstructed using air pluviation method into the shear box, i.e. pouring the dry deposit material with a spoon from nil drop height. The specimens exhibit high porosity (n equals about 0.72) closer than in-situ porosity. The tests are performed in dry condition and all specimens exhibited a dilative behaviour. The friction angle at peak is high, and typical of lapilli clasts ($\phi = 54°$), while the cohesion is null (Table 4). The angle of dilatation (Ψ) is also evaluated and is about 13°. Thus, according to Taylor (1948) the friction angle is about 41°, but it will be reached at large deformation.

Hydraulic conductivity

The mean saturated hydraulic conductivity of the 1888-90 primary deposit measured in the laboratory (8.50×10^{-5} m s^{-1}) is similar to that obtained during field measurements (6.0 and 7.5×10^{-5} m s^{-1}). The mean hydraulic saturated conductivity of the Pal D primary deposit could not be measured in the laboratory because the deposit grainsize (Mdφ = -3.4φ) is too coarse for the apparatus measuring hydraulic conductivity; instead we use here both values one from the literature for other coarse-grained volcanic soils and the second the value obtained through field measurements. A value of 1×10^{-2} m s^{-1} (Table 4) is inferred from the hydraulic conductivity measured in the field on 2011 Cordon Caulle (Chile) eruption lapilli deposits (Baumann et al., 2018) and from the lower pumice deposit from Vesuvius (Crosta and Dal Negro, 2003). These values show a large discrepancy with our field measurements of 6.8 × 10^{-4} m s^{-1}. These two end-members are hereafter referred to as *high* (i.e. 1 × 10^{-2} m s^{-1}) and *low* (i.e. 6.8 × 10^{-4} m s^{-1}) hydraulic conductivities.

Soil Water Retention Curve

The SWRC of the 1888-90 primary deposit exhibit air entry value equal to 1 kPa, while the water content at saturation (θ_s) is 0.47 and the residual water content (θ_r) is 0.04. The SWRC of Pal D deposit exhibit air entry value lower than 1 kPa and slightly high water content at saturation (θ_s = 0.72) and low residual water content (θ_r = 0.03). The data are interpolated using both Gardner (1958) and Brooks and Corey (1962, 1964) equations (Table 4).

Saturated soil diffusivity

The saturated soil diffusivity of the 1888-90 and Pal D primary deposits are one order of magnitude higher than their saturated soil conductivity (Table 4). The 1888-90 primary deposit shows a value of 3.28 × 10^{-4} m^2 s^{-1} the Pal D primary deposit a value of 6.59 × 10^{-3} m^2 s^{-1}.

4.3 Modelling

Based on considerations in Section 2.2, TRIGRS simulation are run using only one very-high intensity rainfall scenario of 6.4 mm h^{-1} over 5 hours (i.e., total of 32 mm). Such intensities have occurred twice in 2011 and have been witnessed to cause widespread floods in the Porto flood-plain. This scenario should be considered as a very high/torrential scenario used to investigate the maximum unstable tephra volume. For the Pal D primary deposit, we used two different hydraulic conductivities in order to consider both end-members as described in laboratory analyses (Table 5).

TRIGRS simulations assume that: i) a water table is located at the bottom of the tephra-fallout sequence (lower boundary); and ii) the tephra sequence lies on an impermeable layer. These assumptions are supported by the exposure of the consolidated and impermeable Tufi Varicolori unit on the upper part of the La Fossa cone (Frazzetta et al., 1983; Capaccioni and Coniglio, 1995; Dellino et al., 2011).

Although lahars have been initiated all around the La Fossa cone in the past, we analyse here the slope and the stability condition of the tephra deposits in two potential lahar source areas (Fig. 7, black lines). The first NW source area represents a direct threat to the populated Porto village, while the second S source area is downwind of the prevailing wind and presents the highest probabilities of tephra accumulations (Section 1.2; Biass et al., 2016). The percentage of slope angle ranges (Fig. 7) for the NW and S lahars source area respectively are 18% and 22% for a slope angle between 6° and 30°; 38% and 46% for slope angle between 30° and 35°; 31% and 24% for slope angles between 35° and 41°; and 12% and 7 % for slope angles bigger than 41°. Comparing the slope angle distribution for both areas, we observe that the percentage of steep slopes is higher in the NW area. Finally, we selected two upper catchments with the same surface (of 4,665 m^2) in order to facilitate the comparison of remobilized volumes associated with different eruptive conditions (Fig. 7).

4.3.1 Deposition and mobilization scenarios

Vulcanian eruption scenarios

Figure 8 shows the probabilistic isopach maps (for a probability of occurrence of 25%) and the instability maps for eruption durations of 6, 12, 18 and 24 months. For an eruption duration of 6 months, only 4.8% percent of the NW and 6% of the S lahar source areas, respectively, ~~result~~ unstable due to the small tephra-fallout deposit thickness (between 6 and 12 cm) (Fig. 8A). For an eruption duration of 12 months, the unstable areas are significantly higher: 69% for the NW and 81% for the S lahar source areas, respectively, for a tephra-fallout deposit thickness between 14 and 22 cm (Fig. 8B, table 6). For an eruption duration of 18 months the percentage of unstable areas for the NW is also very high (89%) and reached a value of 66% for the S area (Fig. 8C). The percentage of unstable area decreases for an eruption duration of 24 months, with 52% for the NW and 22% for the S, where the tephra-fallout deposit accumulation is more than 35 cm in the case of S source area (Fig. 8D, Table 6). Figure 9 shows the unstable volumes as a function of eruption durations described above calculated for 2 single upper catchments with the same area (4,665 m^2) located in the NW source area (UC NW) and the in the S source area (UC S; Fig. 9). The largest unstable volume is reached for an eruption duration of 18 months, with a volume of 1,105 m^3 for the S upper catchment and 990 m^3 for the NW upper catchment in the case of 25% probability of occurrence scenario (Table 7).

Subplinian eruption scenarios

The same two lahars sources areas were used for the TRIGRS runs using subplinian deposits. Four probabilistic isopach maps were considered (VEI 2 and VEI 3 with 25% and 75% probability of occurrence) and combined with hydraulic conductivities both measured in the field and derived from literature (i.e. $K_s = 1 \times 10^{-2}$ m s^{-1} and $K_s = 6.8 \times 10^{-4}$ m s^{-1}). Using the highest hydraulic conductivity, a VEI 2 eruption with a 25% probability of occurrence results in 79% and 14% of unstable areas in the NW and S flank, respectively (Table 6). A 75% probability of occurrence increases unstable areas to 99% and 97%. On the contrary, considering a VEI 3 eruption with 25% probability of occurrence, only the tephra deposit located on slope > 48° is unstable (2% and 0.02%). A 75% probability shows a 99% of unstable area in the NW and 58% in the S area.

Using the lowest hydraulic conductivity, almost all the deposit resulting from a VEI 2 is unstable (99% of the NW source area and 97% of the S source area) regardless of the probability of occurrence (Table 6). In the case of VEI 3 scenario with a 25% probability of occurrence, a high percentage of the NW source area is unstable (97%) whereas only 25% of the S source area is unstable (Table 6).

The unstable tephra-fallout volumes calculated for the subplinian scenarios for the two single upper catchments NW and S show that the largest volume (2,455 m^3) resulted for the NW upper catchment and the subplinian VEI 3 (25%) scenario with a $K_s = 6.8 \times 10^{-4}$ (i.e. hydraulic conductivity measured in the field)(Table 7, fig. 10).

4.3.2 Parametrization of unstable area based on variable tephra-fallout thickness

In order to characterize the minimum tephra-fallout deposit thickness necessary to trigger lahars on Vulcano, we carried out TRIGRS simulations using the characteristics of the 1888-90 the Pal D primary deposit and increasing deposit thicknesses from 0.1 to 1.1 m, with an interval of 0.05 m. The same rainfall scenario was applied.

The percentage of unstable areas for the NW and S source areas (Fig. 11) shows that the tephra-fallout deposit thickness generating the largest instability for the 1888-90 eruption primary deposit is between 20 and 30 cm. For Pal D primary deposits using the lowest hydraulic conductivity, the unstable percentage area decreases rapidly with an increase in deposit thickness, with virtually the entire deposit being stable beyond a 45 cm thickness. In contrast, when the Pal D primary deposit is simulated with high hydraulic conductivity, almost all of the lahar source area is unstable (98%) for deposit thickness between 10 and 65 cm, after which the fraction of unstable area decreases with increasing tephra thickness.

We have also plotted the total pore pressure and the lowest FS at the end of the rainfall event as a function of deposit thickness for three different slope angles (38°, 35.4° and 30.1°). Fig.12 presents results for the 1888-90 eruption primary deposit and results for the Pal D primary deposit, for both values of $K_{s,}$ are seen in Fig. 13. We simulated two different rainfall events: a rainfall intensity of 6.4 mm h^{-1} with a duration of 5 hours (total rainfall of 32 mm) and a rainfall intensity of 15.5 mm h^{-1} with a duration of 3 hours (rainfall event recorded at Lentia station the 11 November 2017, with a total of 46.5 mm). The total pressure head for the 1888-90 eruption deposit has a maximum at 0.25 m for a 30.1° slope angle and a maximum of 0.3 m for a 38° and 35.4° slope angle (Fig 12a). We also show that there is an unstable window (FS < 1) for thicknesses between 12 cm and 50 cm with a slope of 38°, which with lower slopes is narrower; in the case of a slope of 30.1° the deposit is unstable for thicknesses between 20 and 27 cm (Fig. 12b). We also explored the pressure head and FS for a higher rainfall intensity (I = 15.5 mm h^{-1}), representing the worst rainfall scenario for 2017 (Fig. 12c, d). We observed that the unstable window is larger for the three slope angles, with an upper thickness limit of 35 cm, 50 cm and more than 50 cm for the slope angles 30.1°, 35.4° and 38°, respectively. For the same tephra-fallout deposit the ratio of rainfall intensity and hydraulic conductivity (I/K_s) determines the time to reach the water table (located at the bottom of the deposit in our case study); the rate of rise of water table increases with an increase in I/K_s ratio (Li et al., 2013). In the case of the 1888-90 tephra-fallout deposit, the upper critical thickness for instabilities increases with the increase of rainfall intensity and total rainfall.

For the Pal D primary deposit with high hydraulic conductivity, the pressure head increases with decreasing thickness and reaches a maximum of 0.07 m, 0.08 m and 0.087 m for a tephra thickness of 15 cm (Fig. 13a). In contrast, the total pressure head shows a monotonic increase with increasing deposit thickness for low hydraulic conductivity. In the case of the safety factor for high hydraulic conductivity, only very shallow deposits are unstable and for slope angles of 38° the tephra-fallout deposit with a thickness larger than 20 m is stable. In contrast, the FS is constant in the case of low hydraulic conductivity and is below 1 for deposit thicknesses between 10 cm and 55 cm (Fig. 13b).

For a rainfall intensity of 15.5 mm h^{-1} with a duration of 3 hour (Fig. 13c, d) and with a high hydraulic conductivity, the total pressure head has a higher maximum displaced to higher tephra-fallout deposit thickness and the deposit thickness limit between stable and unstable area is higher (almost 32 cm for a slope angle of 38°) compared with the 6.4 mm h^{-1} rainfall intensity (Fig. 13a, b). In contrast, in the case of the low hydraulic conductivity the total pressure head and the safety factor are the same as the results obtained for the lower rainfall intensity (6.4 mm h^{-1}). The constant factor of safety is the result of the upper boundary of pressure head, which is physically limited at the beta-line (Iverson, 2000; Baum et. al., 2008). The total pore pressure cannot be above the values denoted by a water table at the ground surface (beta-line) and the model calculates the factor of safety with this value, which is the worst condition for instability.

5. Discussion

5.1 Characteristics of lahar source deposits

Grain-size distribution of pyroclastic material is one of the primary factors influencing the type of erosion or failure mechanism in the case of rainfall-triggered lahars (e.g., Manville et al., 2000, Pierson et al., 2013). In this study, critical characteristics of tephra-fallout deposits (i.e. grain-size, hydraulic conductivity and angle of friction) necessary as input for shallow landsliding process modelled with TRIGRS have been analysed for two different eruption scenarios (Vulcanian and subplinian). Overall, the tephra fallout deposits associated with both the 1888-90 Vulcanian eruptions and the subplinian Pal D eruption are relatively internally homogeneous in terms of grain-size and geotechnical properties (Tables 1–5). In contrast, the tephra-fallout sequence associated with the climactic phase of the 2011 Cordón Caulle eruptions (Chile) that also generated post-eruption lahars is characterized by two different layers with contrasting grain-size: lapilli at the base (Units I and II) and ash on the top (Unit III) (Pistolesi et al., 2015). In terms of friction angle, Pal D deposits and lapilli layers I and II of Cordón Caulle eruption are very similar, 54° and 53°, respectively. However, the hydraulic conductivities measured in the field are very different (K_s= 3.9x10^{-2} m s^{-1} and K_s= 6.8x10^{-4} m s^{-1}, respectively). This significant difference in hydraulic conductivities can be due partly to the age and the geological setting of the primary deposits and partly to the use of different measuring techniques. In the case of 2011 Cordón Caulle lapilli (Units I and II) the hydraulic conductivity was measured by filling a plastic tube with an undisturbed sample and saturating the materiel with water. Instead, measurements for the Pal D primary deposit was performed on the outcrop with a single ring permeameter (see Appendix A). Besides, the 2011 Cordón Caulle deposit had only a small layer (10 cm) on the top and 0.7% of fine ash. The Pal D deposit is older (AD 1200), with 7% fine ash and overtopped by almost two meters of younger pyroclastic deposits. The lower hydraulic conductivity of the Pal D deposit compared to the 2011 Cordón Caulle lapilli layers could be due to the migration of small particles from the top and a compaction due to the load of the deposits on the top, which reduced the porosity. In fact, the dry unit weight of the Pal D undisturbed sample and the same a reconstructed sample (without compaction) is 6.63 kN m^{-3} (Table 4) and 6.18 kN m^{-3} respectively, which means a greater porosity (6.7%) for the reconstructed sample. Although the 1888-90 primary deposits have a slightly greater friction angle than the ash layers (Unit III) from the 2011 Cordón Caulle eruption (41° and 38.4°, respectively), the hydraulic conductivities are in the same range. The 1888-90 primary deposit also has similar friction angles and hydraulic conductivities with respect to the pyroclastic deposits (ash soil class B) from Vesuvius (Cascini et al., 2010).

Table 8 shows a detailed comparison of grainsize, hydraulic conductivity and infiltration capacity associated with various tephra-fallout and PDC deposits that have generated rain-triggered lahars; annual precipitation for the associated region is also reported. It is important to note that infiltration capacity and hydraulic conductivity can be considered as similar parameters for the sake of this comparison. In fact, the infiltration capacity is a measure of the rate at which soil is able to absorb water (Horton, 1945), while the hydraulic conductivity measures the ease with which water will pass through a porous media (Darcy, 1856). Infiltration capacity typically decreases through time and converges to a constant value, which is the hydraulic conductivity. Infiltration capacity is more easily measured in the field, while hydraulic conductivity is more easily measured in the laboratory.

Examples of lahar generation enhanced by fine-grained deposits include Mt. St Helen 1980 (Leavsley et al., 1989), Chaitén 2008 (Pierson et al., 2013) and Cordon Caulle 2011 (Pistolesi et al., 2015) (Table 8). In contrast, the grainsize of the 1888-90 eruption deposit is closer to Mt. Unzen PDC and Pinatubo tephra. Hydraulic conductivity associated with the 1888-90 eruption deposit is 44 times higher than the infiltration capacity of the PDC in Shultz Creek (Mt. St. Helen). Infiltration capacity is low also in the case of Mt. Unzen, but is higher for the PDCs of Mt. Pinatubo. An important difference between the deposits studied in this paper and the other deposits is the climatic conditions (Table 8): semi-arid, poorly vegetated regions with non-permanent streams and limited annual rainfall (500 mm), such as in the case of Vulcano, versus forested areas with permanent streams draining the volcano flanks and annual precipitation between 1000 mm and until 4300 mm for all other cases.

Grain-size of tephra-fallout deposits directly affect the hydraulic conductivity and infiltration capacity of the deposits. The highest hydraulic conductivities (1×10^{-2}) for Mdϕ < -1ϕ (lapilli) and the lowest hydraulic conductivities and infiltration capacities (between 5×10^{-5} and $1.9\text{x}10^{-6}$) result for Mdϕ > 1 (coarse and fine ash), except for the PDC in Mt. Unzen where Mdϕ is between -1 and 1ϕ (Table 8). In the case of Mt. Unzen, the poor infiltration capacity is not due to fine grain-size but to the development of an impermeable crust on the top of the deposit (Yamakoshi et al., 2000). The combination of hydraulic conductivity (or infiltration capacity) and rainfall intensity influences the lahars triggering mechanism either in terms of slope failure or erosion (Cuomo and Della Sala, 2013). If hydraulic conductivity exceeds rainfall intensity only infiltration occurs, but if rainfall intensity exceeds hydraulic conductivity runoff (overland flow) occurs (Cuomo and Della Sala, 2013; Pierson et al., 2014).

5.2 Short versus long-lasting eruptions

The duration of a long-lasting eruption plays an important role in the pattern of remobilization of tephra-fallout deposits. Different unstable volumes calculated with TRIGRS were obtained for durations of Vulcanian eruptive cycles between 3 and 24 months without considering remobilisation in between the eruptive cycles. The results show that for an eruption time of 18 months and a probability of occurrence of 25% (corresponding to a tephra-fallout deposit thickness between 17 and 33 cm) the unstable areas, and, therefore, the remobilised volumes from the lahar source areas, reached a maximum (1,105 m^3 for the S upper catchment and 990 m^3 for the NW upper catchment). For the eruption duration of 24 months, the increase of tephra-fallout deposit thickness (between 21 and 42 cm) produced a decrease of unstable areas (95 m^3 for the S upper catchment and 861 m^3 for the NW upper catchment). It is worth noting also that the thickness deposit affects both the driving and resisting forces along the slip surface at the bedrock contact. In addition a higher soil thickness also increases the time for rainfall to produce significant changes in pore water pressure at the bedrock contact. Thus, a lower volume of mobilized material may occur despite a thicker deposit. The results obtained with TRIGRS showed that there is an unstable window of tephra-fallout deposit thickness, which depends on amount and duration of rainfall, slope angle and geotechnical characteristics of the deposit. These results are similar to the window of potentially unstable soil thickness found by Dietrich et al. (2007) for a slope stability model that include shear resistance due to lateral and basal boundaries as a result of combination of cohesion (soil and root cohesion) and friction.

The morphology of the middle and the upper part of the La Fossa cone evidence a strong remobilisation of the 1888-90 eruption tephra-fallout deposit. The coarse-ash grainsize range and medium permeability of the 1888-90 tephra fallout deposits in combination with the impermeable deposits at the base of the sequence (i.e., Tufi Varicolori) make this deposit easily remobilised by rainfall through a shallow landslide initiation mechanism. Deep channels due to the continuous remobilisation of this deposit can be observed on the cone (Fig. 1). Because of the short transport distance (200-400 m) the lahar deposits on the La Fossa cone have almost the same grainsize as the 1888-90 tephra fallout deposits (Fig. 6B). The same relation between the primary pyroclastic deposits and the lahars has been described for the la Cuesta succession (Valentine et al., 1998).

Field evidence for post Pal D remobilisation and lahar deposits are not recorded in the stratigraphic record (Di Traglia, 2011). This is consistent with our modelling results with $K_s = 1 \times 10^{-2}$ m s^{-1} that shows the low potential of remobilization associated with thick lapilli deposits. In this case, a high hydraulic conductivity allows the water to rapidly migrate down to the water table with low transient pressure. Therefore, the water table rarely rises sufficiently to induce instability, which explains why thicker deposits are relatively less unstable. In fact, the thick lapilli deposits associated with both VEI 2 and 3 and a high permeability are stable even for the largest rainfall event occurring in Vulcano, e.g. VEI 3 and 25% probability of occurrence (Fig. 10 and table 6). Studies on rainfall lahar generation in Mayon volcano, Philippines also demonstrated that coarse and high permeability pyroclastic deposits on volcano slopes remain stable in most cases (Rodolfo and Arguden, 1991). A similar case occurred at Mt. St. Helen, where rainfall-induced lahar drastically dropped when the erosion of fine ash exposed coarser and more permeable material (Collins and Dunne, 1986).

5.3 Initiation mechanisms of rain-triggered lahars

The tephra mobilization model used in our study assumes rainfall-induced shallow landslides caused by the infiltration of rain on the slope surface. These shallow landslides can eventually transform into lahars depending on the availability of water, slope morphology and characteristics of tephra deposits. In particular, we studied the cases in which rainfall intensity

(I) is lower than hydraulic conductivity (*Ks*) and infiltration occurs before runoff (Cuomo and Della Sala, 2013). At Vulcano, both 1888-90 and the Pal D deposits have high permeability compared to the cases of Mt. St. Helen 1980 and Chaitén 2008 fine-grained tephra-fallout deposits (Table 3). The fine-grained tephra-fallout deposits reduce infiltration capacity on basin slopes, enhancing runoff and producing larger peak flows. However, we cannot discard the mechanism of sheet and rill erosion in Vulcano, which was not simulated in this study. The physical characteristics of primary tephra-fallout deposits (e.g. high hydraulic conductivity) and the rainfall characteristics in Vulcano indicate that the main lahar initiation mechanism is most likely shallow landsliding.

The relationship between unstable areas and deposit thicknesses suggest a significant influence of the hydraulic conductivity on the model outcomes and on the resulting estimation of unstable volumes (Fig. 8 and Tables 6 and 7). Our results better explain the parameter values affecting slope instability (Fig. 11 and Tables 6 and 7). In fact, the tephra-fallout deposit thickness of 21-33 cm associated with the largest unstable volumes for the Vulcanian scenarios (18- and 24-months durations), well correlate with the thickness of 20-30 cm shown in Figure 11. Similarly, the tephra-fallout deposit thickness associated with the largest unstable volumes for the VEI 2 and 3 scenarios (with Ks derived from literature, i.e. 1×10^{-2} m s^{-1}), i.e. 8-25 cm, also shows how a higher hydraulic conductivity generates lahars for lower deposit thickness. These values of tephra-fallout deposit thickness are in good agreement with the critical threshold for the lahar generation found by Sulpizio et al. (2006) for syn-eruptive lahars in the Vesuvian area (i.e. 10 cm).

For the 1888-90 primary tephra, results suggest that cohesion leads to a critical minimum landslide depth size (lower limit deposit thickness for instability) dependent on the slope angle (Fig. 12b, d). Using a model for natural slopes, Milledge et al. (2014) found a critical depth in cohesive soil, resulting in a minimum size for failure. For cohesionless material, such as the primary Pal D, the lower thickness limit is not defined as most small deposit thickness are unstable, and become progressively stable with deposit thickness increase depending on rainfall intensity and duration and slope angle (Fig. 13b, d).

The different behaviour for all modelled tephra-fallout deposits could relate to the fact that rainfall-induced slope failure can occur by two mechanisms (Li et al. 2013): 1) rainfall infiltration produces a rise of groundwater, which generates positive pore pressure and adds weight on the slope (Cho and Lee, 2002; Crosta and Frattini, 2003; Soddu et al., 2003); 2) rainfall results in a propagation of wetting front causing an increase in water content and pore pressure (loss in matric suction) (Ng et al., 2001; Collins and Znidarcic, 2004; Rahardjo et al., 2007).

First, in the case of subplinian tephra-fallout deposit with $K_s = 6.8 \times 10^{-4}$ m s^{-1} (low conductivity), wetting front mechanism moves from the ground surface toward the bedrock, which means that the time for the perturbation to reach the bedrock contact increases with deposit thickness. As a result, for the same rainfall, the higher the thickness the more stable the slope (Fig. 11, green curve). Second, in the case of subplinian tephra-fallout deposit with $K_s = 1 \times 10^{-2}$ m s^{-1} (high conductivity) the water moves fast down to the water table with low transient pressure (a sort of drained conditions). This means that the water table should be the same provided by the same rainfall, independently from the total deposit thickness. The slope is very sensitive to the ratio of water table/total thickness and becomes stable with the increase of deposit thickness. Finally, in the case of the 1888-90 tephra-fallout deposit, the right side of the curve could be explained by both mechanisms of green and orange curves (Fig. 11), but for the left side for small deposit thicknesses the pore pressure reached at the end of the rainfall is not enough to neutralize the effect of cohesion (0.5 kPa).

The results obtained with the TRIGRS model show the potential for the evaluation of transient pore-water pressure stability condition and lahar (landslide) source areas during rainfall (Godt et al., 2008), even though the role of suction in unsaturated condition, which plays a fundamental role for the pore pressure regime, is not included in the model (Sorbino et al., 2010). Matrix suction between 24 and 27 kPa were measured in 1888-90 primary tephra deposits in May 2018 (at the beginning of the dry season), but further seasonal matrix suction variation needs to be performed to evaluate the role of suction in potential unstable areas evaluation and the most critical period for slope stability (Pirone et al., 2016)

5.4 Impact and risk implications

Remobilised tephra-fallout volume has been calculated with TRIGRS for two different catchments with same area, one located on the NW flank and the other on S flank of La Fossa volcano. We obtained different volumes for the two catchments for the same eruption scenarios (Figs. 8 and 10). Two main factors are responsible for these differences in volume. The first factor is that the tephra deposit is thicker for the S flank due to the prevailing wind direction to the SE and, therefore, it inhibits the formation of lahars as it requires more water to be remobilized (which is not frequently available in the Vulcano area). In fact, there is a thickness threshold for instability depending on rainfall intensity and tephra-fallout deposit properties (Fig. 13). An additional factor influencing the deposit stability is the slope morphology. Steep slope (> 35°) are more frequent in the NW flank, with 42% for the NW basin and 32% for the S basin, which explains a higher percentage of unstable area for the NW part. As a result, due both to the lower deposit thickness and to the steeper slopes, the NW flank is more likely to generate lahars than the S flank, even though lahars from the S flank are also significant (Fig. 10). It is important to consider that one of the most populated part of the island (i.e., Porto Village; Galderisi et al., 2011), which is also where the key infrastructures are located, is directly exposed to the lahars potentially generated on the NW flank of the volcano. In contrast, the residential area of Piano located on the S of the island is protected by caldera rim that could easily block all lahars forming on the S flank. It is also important to highlight the importance of assessing the effect of compounding hazards in the case of multi-hazard environments such as volcanic eruptions. In fact, volcanic hazards are often assessed individually, while investigation of the associated cascading effects such as for tephra sedimentation and lahars should be considered (e.g. Tierz et al. 2017). In fact, our results demonstrate the effectiveness and strength of combining probabilistic tephra hazard modelling with lahar-triggering modelling. The next step necessary to assess the impact of the combination between tephra sedimentation and lahar propagation is lahar-inundation modelling. Clearly, each step requires dedicated studies and investigations and has some intrinsic value on its own; however, the combination of all aspects has a tremendous potential for the impact assessment of communities developed in volcanic areas.

6. Conclusions

We presented a detailed analysis of the volume of tephra-fallout deposit that could be potentially remobilized by rainfall as a result of two eruptive scenarios of La Fossa volcano, the main volcanic system on Vulcano island: a long lasting Vulcanian eruption (i.e., using the 1888-90 eruption as the reference event) and a short-lived eruption (VEI 2 and VEI 3; using the Pal D eruption as the reference event). The great novelty of this work is the assessment of compounding hazards (tephra-fallout deposits and lahar triggering) based on both numerical modelling and field characterization. We demonstrate that an accurate assessment of unstable areas can only be obtained based on a combination of dedicated numerical simulations and detailed field and geotechnical studies. In fact, volumes of tephra-fallout deposit that could be remobilized by rain-triggered lahars were analyzed using a slope stability model (TRIGRS) in combination with field observations and geotechnical tests. In particular, we have considered 12 probabilistic isopach maps with different eruption duration and probabilities of occurrence of 25% and 75% in the case of the Vulcanian eruptive scenario. We have also considered 4 probabilistic isopach maps with two different VEI (2 and 3) and the same probabilities of occurrence in the case of subplinian eruptive scenario. In addition, a parametric analysis was performed with TRIGRS to determine the tephra fallout thickness thresholds required to trigger lahars for a given rainfall event. Two basins of same area were identified on the NW and S flank of the volcano to analyse the effect of different morphology and of different accumulation related to the prevailing wind direction. The results of unstable volumes for the two basins located show that:

1) for the Vulcanian scenario, the largest unstable volume is reached for an eruption duration of 18 months and a 25% probability of occurrence scenario, with a volume of 1,105 m3 for the S basin and 990 m3 for the NW basin;
2) for the subplinian scenario, the largest unstable volume (2,455 m3) resulted for the VEI3 (25% of occurrence) with a Ks= 6.8 × 10-4 m s-1 (i.e. hydraulic conductivity measured in the field) in the case of the NW basin;
3) for the subplinian scenario with Ks= 1 × 10-2 m s-1 (i.e. hydraulic conductivity estimated from literature) the largest unstable volume (563 m3) was found for the NW basin with a scenario VEI2 (25% of occurrence).

The parametric analysis with variable tephra-fallout thickness and slope and two rainfall events of 6.4 mm h^{-1} for 5 hours and 15. 5mm h-1 for 3 hour shows that:

4) for a tephra-fallout deposit with features associated with a Vulcanian eruption, the thickness generating the largest instability is between 20 and 25 cm for 6.4 mm h^{-1} and between 20 and 35 cm for 15.5 mm h^{-1};
5) for a tephra-fallout deposit with features associated with a subplinian eruption with K_s= 1 × 10^{-2} m s^{-1}, the unstable area percentage decreases rapidly with an increase in deposit thickness, being all the area almost stable beyond a 45 cm thickness;
6) for a tephra-fallout deposit with features associated with a subplinian eruption with K_s= 6.8 × 10^{-4} m s^{-1}, almost all the lahar source area results unstable (98%) between 0.1 and 0.65 m deposit thickness; beyond 0.65 m the fraction of unstable area decreases with the increase in tephra thickness increase for the rainfall of 6.4 mm h^{-1};
7) for a tephra-fallout deposit with features associated with a Vulcanian eruption we observe an unstable window with

Nat. Hazards Earth Syst. Sci. Discuss., https://doi.org/10.5194/nhess-2019-77
Manuscript under review for journal Nat. Hazards Earth Syst. Sci.
Discussion started: 10 April 2019

a minimum thickness for instability and suggest that cohesion leads to a critical minimum landslide depth dependent on the slope angle. Instead, cohesionless material such as the primary Pal D deposit is unstable for all small deposit thickness values and a low thickness limit was not reached; the tephra-fallout deposit becomes stable with thickness increase depending on rainfall and slope angle.

The results modelled with TRIGRS show that shallow landsliding is an effective process for eroding both Vulcanian-type and subplinian-type (with $K_s = 6.8 \times 10^{-4}$ m s^{-1}) tephra-fallout deposits in combination with high-intensity rainfall events with short duration, such as those occurring in Vulcano every year. Nonetheless, the occurrence of shallow landsliding is a complex process (e.g., Table 7 and Fig. 10 and 13) and the tephra fallout deposit thickness threshold strongly depends on rainfall intensity, tephra-fallout deposit characteristics and geomorphology features. Both eruptive scenarios (e.g., plume height, erupted mass, eruption duration) and prevailing wind direction are, therefore, crucial to the generation of rain-triggered lahars, having a first order control on tephra-fallout deposit thickness. Physical characteristics of tephra-fallout deposits (e.g. hydraulic conductivity, grainsize and cohesion) and geomorphological features (e.g. flank slopes), the characteristics of soil at the base of the deposits and vegetation are also important parameters to consider as they have a first order control on slope instability. We can conclude that deposit thickness and rainfall intensity alone are not sufficient to derive thresholds for lahar triggering; a comprehensive assessment of unstable volumes that could potentially trigger lahars, in fact, requires dedicated numerical simulations combined with detailed field observations and geotechnical analysis as we did in this study.

Data availability

Most data is made available in tables. Additional data is available upon request, based on a collaborative agreement.

Appendix

Appendix A: Field strategies

Sampling of undisturbed deposit for geotechnical tests

Undisturbed tephra-fallout deposit is sampled for testing the properties in the laboratory, without disturbing structure texture, density, natural water content and stress condition (Figs A1a and b). Sampling was performed by inserting a steel tube 3 mm thick with a height of 30 cm and a diameter of 10 cm into the ground (Fig. A1a). After that, we cleaned all the deposit around the tube to extract it with a minimum disturbance. Then, a support was inserted at the base of the cylinder, and the tube was extracted from the deposit. Finally, the tube was covered on both ends with a plastic cover and plastic tape to preserve the deposit for disturbance during the transport (Fig. A1b).

Soil suction measurement

Soil suction measurements were carried out in situ on the 1888-90 tephra-fallout deposit with a soil moisture probe ("Quick Draw" Model 2900FI) (Fig. A2b). The first step in taking a reading with the probe is to core a hole pushing the coring tool into the soil (Fig. A2a). After removing the coring tool we have a proper sized hole to insert the probe. The second step is to insert the probe in the soil and wait approximately one minute (equalization time assessed for such soils). Finally, the suction can be read on the dial gauge (Fig. A2b). The soil suction is created by water capillary pressure that each soil particle applies into the soil. The moisture probe has a porous ceramic sensing tip at the end of the tube. The soil suction reading is obtained when a small amount of water transfers between the sensing tip of the probe and the soil.

Saturated hydraulic conductivity measurement

The saturated hydraulic conductivity was estimated in the field with a single-ring permeameter for both deposits (Figs A3a and b). The apparatus for the measurements consists of a steel ring with diameter of 21 cm and height of 12 cm, a plastic cover with a hole to insert a Mariotte bottle (Fig. A3b). In the field, we put the ring on a horizontal plane surface on the tephra-fallout deposit. Then, the first 6 cm were pushed into the ground. Finally, we filled the Mariotte bottle with water and inserted it on the tape turned upside-down. The water first formed a 1 cm layer on the tephra-fallout deposit and then started to infiltrate into the deposit. For the infiltration rate measurements the readings were done every minute in the case of 1888-90 eruption deposit and every 30 seconds in the case of Pal-D deposit. The duration of the measurements was 40 minutes for 1888-90 deposit and 3.2 minutes for the pal-D deposit.

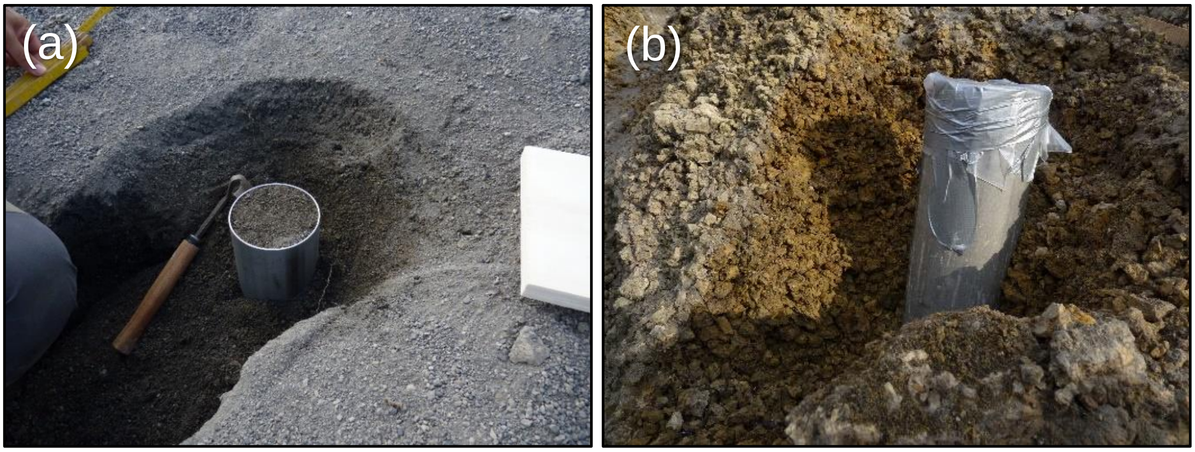

Figure A1: a) Sampling the 1888-90 AD tephra sequences with a 30 cm steel tube. We clean all the deposit around the tube to extract it with a minimum disturbance. B) Sampling the Pal-D deposit with a 30 cm steel tube. The tube is covered with a plastic cover and plastic tape before to extract the tube from the deposit with a basal support.

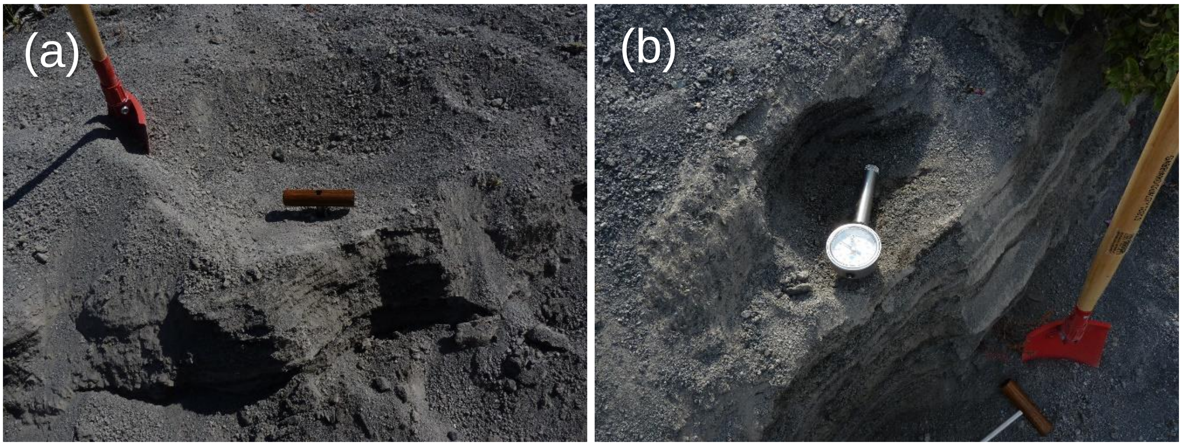

Figure A2: a) Coring tool into the soil before soil suction measurement b) Soil suction measurement on the 1888-90 primary deposit on the NW volcano flank.

Figure A3: a) Ring infiltrometer, 6 cm are buried into the 1888-90 primary deposit. b) Ring infiltrometer during the infiltration measurements. With the bottle turned upside-down with water infiltrating in the ground.

Competing interests

The authors declare that they have no conflict of interest.

Acknowledgments

The authors are grateful to Irene Manzella, Michel Jaboyedoff, and Mario Sartori for constructive discussion and to Corine Frischknecht, Mauro Rosi and Ramon Arrowsmith for discussion and assistance in the field. The work was supported by the by the Swiss National Science Foundation (#200021_163152). M.P. was supported by a project "PRA 2018-19 (Progetti di Ricerca di Ateneo)" granted by University of Pisa.

References

Arnone E., Pumo D., Viola F., Noto L.V., La Loggia G.: Rainfall statistics changes in Sicily. Hydrol Earth Syst Sci 17(7): 2449–2458, doi:10.5194/hess-17-2449-2013, 2013.

Arrighi S., Tanguy J.C., Rosi M.: Eruptions of the last 2200 years at Vulcano and Vulcanello (Aeolian Islands, Italy) dated by high-accuracy archeomagnetism. Phys Earth Planet Inter 159(3–4): 225–233, 2006.

Aubertin et al. (2003) Aubertin, M., Mbonimpa, M., Bussière, B., Chapuis, R.P.: A model to predict the water retention curve from basic geotechnical properties. Can. Geotech. J. 40, 1104–1122, doi:10.1139/t03-054, 2003.

Baum, R. L., Savage, W. Z., Godt, J. W.: TRIGRS—a Fortran Program for Transient Rainfall Infiltration and Grid-Based Regional Slope-Stability Analysis. US geological survey open-file report, 424, 38, 2002.

Baum, R. L., Savage, W. Z., Godt, J. W.: TRIGRS — A Fortran Program for Transient Rainfall Infiltration and Grid-Based Regional Slope-Stability Analysis, Version 2.0. U.S. Geological Survey Open-File Report, (2008–1159), 75, doi:Open-File Report 2008–1159, 2008.

Baumann, V., Bonadonna, C., Cuomo, S., Moscariello, M., & Manzella, I.: Slope stability models for rainfall-induced lahars during long-lasting eruptions. Journal of Volcanology and Geothermal Research, 359, 78–94, doi:10.1016/j.jvolgeores.2018.06.018, 2018

Biass, S., Bonadonna, C., Di Traglia F., Pistolesi M.,Rosi, M., & Lestuzzi, P.: Probabilistic evaluation of the physical impact of future tephra fallout events for the Island of Vulcano, Italy. *Bulletin of Volcanology*, doi:10.1007/s00445-016-1028-1, 2016.

Bisson, M., Favalli, M., Mazzarini, F., Mori, A., Pareschi, M. T., & Sinapi, L.: A morphometric model of the Aeolian Islands (Italy). NUOVO CIMENTO-SOCIETA ITALIANA DI FISICA SEZIONE C, *26*(4), 417-436, 2003.

Capaccioni, B., & Coniglio, S.:Varicolored and vesiculated tuffs from La Fossa volcano, Vulcano Island (Aeolian Archipelago, Italy): evidence of syndepositional alteration processes. *Bulletin of Volcanology*, *57*(1), 61-70, 1995.

Cascini, L., Cuomo, S., Pastor, M., Sorbino, G.: Modeling of Rainfall-Induced Shallow Landslides of the Flow-Type. J. Geotech. Geoenvironmental Eng. 136, 85–98, doi:10.1061/(ASCE)GT.1943-5606.0000182, 2010.

Cascini, L., Cuomo, S., Della Sala, M.:Spatial and temporal occurrence of rainfall-induced shallow landslides of flow type: A case of Sarno-Quindici, Italy. Geomorphology 126, 148–158, doi:10.1016/j.geomorph.2010.10.038, 2011.

Charbonnier, S.J., Connor, C.B., Connor, L.J., Sheridan, M.F., Oliva Hernández, J.P., Richardson, J.A.: Modeling the October 2005 lahars at Panabaj (Guatemala). Bull. Volcanol. 80, doi:10.1007/s00445-017-1169-x, 2018

Cho, S.E., Lee, S.R.: Evaluation of surficial stability for homogeneous slopes considering rainfall characteristics. Journal of Geotechnical and Geoenvironmental Engineering 128, 756–763, 2002.

Collins, B. D., & Dunne, T.: Erosion of tephra from the 1980 eruption of Mount St. Helens. Geol. Soc. Am. Bull. 97, 896–905, 1986.

Collins, B. D., & Znidarcic, D.: Stability analyses of rainfall induced landslides. Journal of geotechnical and geoenvironmental engineering, 130(4), 362-372, 2004.

Crosta, G. B., & Frattini, P.: Distributed modelling of shallow landslides triggered by intense rainfall. Natural Hazards and Earth System Science, 3(1/2), 81-93, 2003.

Crosta, G.B., Dal Negro, P.: Observations and modelling of soil slip-debris flow initiation processes in pyroclastic deposits: the Sarno 1998 event. Nat. Hazards Earth Syst. Sci. 3, 53–69, doi:10.5194/nhess-3-53-2003, 2003.

Cuomo, S., Della Sala, M.: Rainfall-induced infiltration, runoff and failure in steep unsaturated shallow soil deposits. Engineering Geology, *162*, 118–127, doi:10.1016/j.enggeo.2013.05.010, 2013.

Cuomo, S., Della Sala, M., Novità, A.: Physically based modelling of soil erosion induced by rainfall in small mountain basins. Geomorphology 243, 106–115, doi:10.1016/j.geomorph.2015.04.019, 2015.

Cuomo, S., Chareyre, B., d'Arista, P., Della Sala, M., & Cascini, L.: Micromechanical modelling of rainsplash erosion in unsaturated soils by Discrete Element Method. Catena, 147, 146-152, 2016.

Cuomo, S., Iervolino, A.: Investigating the role of stratigraphy in large-area physically-based analysis of December 1999 Cervinara shallow landslides. Journal of Mountain Science, 13(1), 104-115, 2016.

De Astis, G., La Volpe, L., Peccerillo, A., Civetta, L.: Volcanological and petrologicalevolution of Vulcano Island (Aeolian Arc, Southern Tyrrenian Sea). Journal of Geophysical Research 102, 8021–8050, 1997.

De Astis G., Lucchi F., Dellino P., La Volpe L., Tranne C.A., Frezzotti M.L., Peccerillo A.: Chapter 11 Geology, volcanic history and petrology of Vulcano (central Aeolian archipelago). Geological Society, London, Memoirs 37(1):281–349, doi:10.1144/M37.11.http://mem.lyellcollection.org/content/37/1/281.abstract, 2013.

De Bélizal, E., Lavigne, F., Hadmoko, D. S., Degeai, J. P., Dipayana, G. A., Mutaqin, B. W., ... & Vidal, C.: Rain-triggered lahars following the 2010 eruption of Merapi volcano, Indonesia: A major risk. Journal of Volcanology and Geothermal Research, 261, 330-347, 2013.

De Fiore O.: Vulcano (isole eolie). In: Friedlaender I (ed) Revisita vulcanologica (suppl. 3), pp 1–393, 1922.

Daag, A.S.: Modelling the erosion of pyroclastic flow deposits and the occurrences of lahars at Mt. Pinatubo, Philippines. Unpublished PhD thesis, ITC Dissertation number 104. Utrecht: Univesity of Utrecht, 2003.

Darcy, H.: Les fontaines publiques de la ville de Dijon : exposition et application des principes à suivre et des formules à employer dans les questions de distribution d'eau, *Victor* Dalmont, Paris, 1856.

Dee, D. P., Uppala, S. M., Simmons, A. J., Berrisford, P., Poli, P., Kobayashi, S., . S, Andrae U, Balmaseda MA, Balsamo G, Bauer P, Bechtold P, Beljaars ACM, van de Berg L, Bidlot J, Bormann N, Delsol C, Dragani R, Fuentes M, Geer AJ, Haimberger L, Healy SB, Hersbac, H, Hólm EV, Isaksen L, Kallberg P, Köhler M, Matricardi, M, McNally AP, Monge-Sanz BM, Morcrette JJ, Park BK, Peubey, C, de Rosnay P, Tavolato C, Th´epaut JN, Vitart F (.. & Bechtold, P.: The ERA-Interim reanalysis: Configuration and performance of the data assimilation system. *Quarterly Journal of the royal meteorological society*, *137*(656), 553-597, 2011.

De Martonne E.: Une nouvelle fonction climatologique: l’indice d'aridité. La Météorologie, 2, 449 – 458, 1926.

Dellino P., La Volpe L.: Stratigrafia, dinamiche eruttive e deposizionali, scenario eruttivo evalutazioni di pericolosit`a a La

Fossa di Vulcano. Tech. rep., CNR-gruppo Nazionale per la Vulcanologia, Volume speciale Vulcano-Progetto triennale, 1992-1995, 1997.

Dellino, P., De Astis, G., La Volpe, L., Mele, D., & Sulpizio, R.: Quantitative hazard assessment of phreatomagmatic eruptions at Vulcano (Aeolian Islands, Southern Italy) as obtained by combining stratigraphy, event statistics and physical modelling. *Journal of Volcanology and Geothermal Research*, *201*(1-4), 364-384, 2011.

Di Traglia, F.: The last 1000 years of eruptive activity at the Fossa Cone (Island of Vulcano, Southern Italy). PhD thesis. Dipartimento di Scienze della Terra. Scuola di Dottorato di Ricerca in Scienze di Base Galileo Galilei. Programma di Scienze della Terra. Università degli Studi di Pisa, 2011.

Di Traglia, F. Di, Pistolesi, M., Rosi, M., Bonadonna, C., Fusillo, R., & Roverato, M.: Geomorphology Growth and erosion: The volcanic geology and morphological evolution of La Fossa (Island of Vulcano, Southern Italy) in the last 1000 years. *Geomorphology, 194,* 94–107, doi:10.1016/j.geomorph.2013.04.018, 2013.

Dietrich, W., McKean, J., Bellugi, D., Perron, T.: The prediction of shallow landslide location and size using a multidimensional landslide analysis in a digital terrain model. Fourth Int. Conf. Debris-Flow Hazards Mitig. Mech. Predict. Assess. 12, 2007.

Ferrucci, M., Pertusati, S., Sulpizio, R., Zanchetta, G., Pareschi, M. T., & Santacroce, R.: Volcaniclastic debris flows at La Fossa Volcano (Vulcano Island, southern Italy): Insights for erosion behaviour of loose pyroclastic material on steep slopes. *Journal of Volcanology and Geothermal Research*, *145*(3–4), 173–191, doi:10.1016/j.jvolgeores.2005.01.013, 2005.

Frattini, P., Crosta, G.B., Fusi, N., Dal Negro, P.: Shallow landslides in pyroclastic soils: A distributed modelling approach for hazard assessment. Eng. Geol. 73, 277–295, doi:10.1016/j.enggeo.2004.01.009, 2004.

Frazzetta, G., La Volpe, L., & Sheridan, M. F.: Evolution of the Fossa cone, Vulcano. Journal of Volcanology and Geothermal Research, 17, 329-360, 1983.

Frazzetta, G., Gillot, P. Y., La Volpe, L., & Sheridan, M. F.: Volcanic hazards at Fossa of Vulcano: Data from the last 6,000 years. *Bulletin Volcanologique*, *47*(1), 105–124, doi:10.1007/BF01960543, 1984.

Galderisi A., Bonadonna C., Delmonaco G., Ferrara F.F., Menoni S., Ceudech A., Biass S. , Frischknecht C, Manzella I. , Minucci G., Gregg C.: Vulnerability assessment and risk mitigation: the case of Vulcano Island, Italy. Proceedings of the Second World Landslide Forum, 3-7 October 2011, Rome, 2011.

Gardner, W. R.: Some steady-state solutions of the unsaturated moisture flow equation with application to evaporation from a water table. Soil science, 85(4), 228-232, 1958.

Gioncada, A., Mazzuoli, R., Bisson, M., Pareschi, M.T.: Petrology of volcanic products younger than 42 ka on the Lipari-Vulcano complex (Aeolian Islands, Italy): An example of volcanism controlled by tectonics. J. Volcanol. Geotherm. Res. 122, 191–220, doi:10.1016/S0377-0273(02)00502-4, 2003.

Godt, J.W., Baum, R.L., Savage, W.Z., Salciarini, D., Schulz, W.H., Harp, E.L.: Transient deterministic shallow landslide modeling: Requirements for susceptibility and hazard assessments in a GIS framework. Eng. Geol. 102, 214–226, doi:/10.1016/j.enggeo.2008.03.019, 2008.

Horton, R.E.: Erosional development of streams and their drainage basins; hydrophysical approach to quantitative morphology. Geological Society of America Bulletin, 56(3), 275-370, 1945.

Iverson, R.M.: Landslide triggering by rain infiltration. Water Resour. Res. 36, 1897–1910, doi:10.1029/2000WR900090, 2000.

Iverson, R.M., Lahusen R.G.: Dynamic Pore-Pressure Fluctuations in Rapidly Shearing Granular Materials. Am. Assoc. Adv. Sci. 246, 796–799, 1989.

Iverson, R.M., Vallance J.: New views of granular mass flows. Geology; 29 (2):115-118, doi:10.1130/0091-7613(2001)029<3C0115:NVOGMF<3E2.0.CO;2, 2001.

Janda, R., Daag, A., Delos Reyes, P., Newhall, C., Pierson, T., Punongbayan, R., Rodolfo, K.: Assessment and Response to Lahar Hazard around Mount Pinatubo, 1991 to 1993. Fire Mud; Eruptions Lahars Mt. Pinatubo, Philipp. 107–139, 1996.

Keller, J.: The island of Vulcano. Rend. Soc. Italian Miner. Petrol. 36, 369–414, 1980.

Kovács G: Seepage hydraulics. Elsevier Science Publishers, Amsterdam, 1981.

Krumbein, W. C.: Size frequency distributions of sediments and the normal phi curve. Journal of Sedimentary Petrology, 8, 84–90, 1938.

Lanza, R. & Zanella, E.: Paleomagnetic secular variation at Vulcano (Aeolian islands) during the last 135 kyr. Earth and Plane- tary Science Letters, 213, 321–336, 2003.

Lavigne, F., Thouret, J.-C., Voight, B., Young, K., LaHusen, R., Marso, J., Suwa, H., Sumaryono, A., Sayudi, D.., Dejean, M.: Instrumental lahar monitoring at Merapi Volcano, Central Java, Indonesia. J. Volcanol. Geotherm. Res. 100, 457–478, doi:10.1016/S0377-0273(00)00151-7, 2000 a.

Leavesley, G. H., Lusby, G. C., Lichty, R. W.: Infiltration and erosion characteristics of selected tephra deposits from the 1980 eruption of Mount St. Helens, Washington, USA. Hydrological sciences journal, 34(3), 339-353,1989.

Li, W. C., Lee, L. M., Cai, H., Li, H. J., Dai, F. C., & Wang, M. L.: Combined roles of saturated permeability and rainfall characteristics on surficial failure of homogeneous soil slope. Engineering Geology, 153, 105-113, doi:10.1016/j.enggeo.2012.11.017, 2013

Major, J.J., Yamakoshi, T.: Decadal-scale change of infiltration characteristics of a tephra-mantled hillslope at Mount St Helens, Washington. Hydrol. Process. 19, 3621–3630, doi:10.1002/hyp.5863, 2005.

Major, J.J., Pierson, T.C., Dinehart, R.L., Costa, J.E.: Sediment yield following severe volcanic disturbance - A two-decade perspective from Mount St. Helens. Geology 28, 819–822. doi:10.1130/0091-7613(2000)28<819:SYFSVD>2.0.CO;2, 2000.

Manville, V., White, J. D. L., Hodgson, K. A.: Dynamic interactions between lahars and stream flow: A case study from Ruapehu volcano, New Zealand: Discussion and reply: Discussion. Geological Society of America Bulletin, 112(7), 1149-1151, 2000.

Mead, S., Magill, C., Hilton, J., 2016. Rain-triggered lahar susceptibility using a shallow landslide and surface erosion model. Geomorphology 273, 168–177, doi:10.1016/j.geomorph.2016.08.022, 2016.

Mercalli, G., and Silvestri, O.: Le eruzioni dell'isola di Vulcano, incominciate il 3 Augusto 1888 e terminate il 22 Marzo

1880, Ann. Uffic. Cent. Meteorol. Geodin., 10(4), 213 pp, 1891.

Milledge, D.G., Bellugi, D., Mckean, J.A., Densmore, A.L., Dietrich, W.E.: Journal of Geophysical Research : Earth Surface 2481–2504, doi:10.1002/2014JF003135, 2014.

Ng, C. W., Wang, B., & Tung, Y. K.: Three-dimensional numerical investigations of groundwater responses in an unsaturated slope subjected to various rainfall patterns. Canadian Geotechnical Journal, 38(5), 1049-1062, 2001.

Newhall, C. G., & Punongbayan, R. (Eds.): Fire and mud: eruptions and lahars of Mount Pinatubo, Philippines (p. 1126). Quezon City: Philippine Institute of Volcanology and Seismology, 1996.

Newhall C.G., Self S.: The volcanic explosivity index (VEI)—an estimate of explosive magnitude for historical volcanism. J Geophys Res 87(C2):1231–1238, 1982.

INGV(Instituto Nazionale de Geofisica e Vulcanologia) -Palermo https://www.pa.ingv.it/, last access: 7 March 2019.

Pierson T.C.: Hyperconcentrated flow—transitional process between water flow and debris flow. In: Jakob M, Hungr O (Eds). Debris-flow hazards and related phenomena. Springer-Praxis, Chichester, pp 159–202, 2005.

Pierson, T. C., & Major, J. J.: Hydrogeomorphic Effects of Explosive Volcanic Eruptions on Drainage Basins. Annual Review of Earth and Planetary Sciences, *42*(1), 469–507. doi:10.1146/annurev-earth-060313-054913, 2014.

Pierson, T. C., Janda, R. J., Thouret, J. C., & Borrero, C. A.: Perturbation and melting of snow and ice by the 13 November 1985 eruption of Nevado del Ruiz, Colombia, and consequent mobilization, flow and deposition of lahars. Journal of Volcanology and Geothermal Research, 41(1), 17-66, 1990.

Pierson, T.C., Janda, R.J., Umbal, J. V, Daag, a S.: Immediate and long-term hazards from lahars and excess sedimentation in rivers draining Mount Pinatubo, Philippines. U.S. Geol. Surv. Water-Resour. Invest. Rep pp, 92–403937, 1992.

Pierson, T.C., Major, J.J., Amigo, Á., Moreno, H.: Acute sedimentation response to rainfall following the explosive phase of the 2008-2009 eruption of Chaitén volcano, Chile. Bull. Volcanol. 75, 1–17. doi:10.1007/s00445-013-0723-4, 2013.

Pirone, M., Papa, R., Nicotera, M. V., & Urciuoli, G.: Analysis of safety factor in unsaturated pyroclastic slope. In Landslides and Engineered Slopes. Experience, Theory and Practice, pp. 1647-1654, CRC Press, 2016.

Pistolesi, M., Cioni, R., Bonadonna, C., Elissondo, M., Baumann, V., Bertagnini, A., Chiari, L., Gonzales, R., Rosi, M., Francalanci, L.: Complex dynamics of small-moderate volcanic events: the example of the 2011 rhyolitic Cordón Caulle eruption, Chile. Bull. Volcanol. 77, doi:10.1007/s00445-014-0898-3, 2015.

Rahardjo, H., Ong, T. H., Rezaur, R. B., & Leong, E. C.: Factors controlling instability of homogeneous soil slopes under rainfall. *Journal of Geotechnical and Geoenvironmental Engineering*, *133*(12), 1532-1543, 2007.

Rodolfo, K. S., & Arguden, A. T.: Rain-lahar generation and sediment delivery systems at Mayon Volcano, Philippines, 1991.

Rossi, G., Catani, F., Leoni, L., Segoni, S., & Tofani, V.: HIRESSS: a physically based slope stability simulator for HPC applications. Natural Hazards and Earth System Sciences, 13(1), 151-166, 2013.

Savage, W. Z., Godt, J. W., Baum, R. L.: A model for spatially and temporally distributed shallow landslide initiation by rainfall infiltration. In:3rd International Conference on Debris-Flow Hazards Mitigation: Mechanics, Prediction, and

Assessment, Vol. 1, pp. 179-187, 2003.

Savage, W. Z., Godt, J. W., Baum, R. L.: Modeling time-dependent areal slope stability. Landslides: evaluation and stabilization. Balkema, Taylor & Francis Group, London, 23-38, 2004.

Salciarini, D., Godt, J.W., Savage, W.Z., Conversini, P., Baum, R.L., Michael, J.A.: Modeling regional initiation of rainfall-induced shallow landslides in the eastern Umbria Region of central Italy. Landslides 3, 181–194, doi:10.1007/s10346-006-0037-0, 2006.

Scott, W.E., Hoblitt, R.P., Torres, R.C., Self, S., Martinez, M.L., Nillos, T.: Pyroclastic flows of the June 15, 1991, climactic eruption of Mount Pinatubo. Fire Mud eruptions lahars Mt. Pinatubo. Philipp. 545–570, 1996.

Scott, K.M., Vallance, J.W., Kerle, N., Macías, J.L., Strauch, W., Devoli, G.: Catastrophic precipitation-triggered lahar at Casita volcano, Nicaragua: Occurrence, bulking and transformation. Earth Surf. Process. Landforms 30, 59–79. doi:10.1002/esp.1127, 2005.

Soddu, S., Delitala, G., Sciabica, M., & Barrocu, G.: Modelling groundwater effects on slope stability. Materials and Geoenvironment, *50*, 349-352, 2003.

Sorbino, G., Sica, C., Cascini, L., & Cuomo, S.: On the forecasting of flowslides triggering areas using physically based models. In Proceedings of 1st North American landslides conference AEG Special Publication, Vol. 1, pp. 305-315, 2007.

Sorbino, G., Sica, C., Cascini, L.: Susceptibility analysis of shallow landslides source areas using physically based models. Nat. Hazards 53, 313–332. doi:10.1007/s11069-009-9431-y, 2010.

Srivastava, R., & Yeh, T. C. J.: Analytical solutions for one-dimensional, transient infiltration toward the water table in homogeneous and layered soils. Water Resources Research, 27(5), 753-762, 1991.

Sulpizio R., Zanchetta G., Demi F., Di Vito M.A., Pareschi M.T. and Santacroce R.: The Holocene syneruptive volcaniclastic debris flows in the Vesuvian area: Geological data as a guide for hazard assessment, in Siebe, C. Macias, J.L. and Aguirre-Díaz., eds. Neogene-Quaternary continental margin volcanism: A Perspective from México: Geological Society of America Special paper 402,p 203-221, doi:10.1130/2006.2402(10), 2006.

Taylor, D.: Fundamentals of soil mechanics. Chapman and Hall, Limited; New York, 1948.

Thouret, J. C., Abdurachman, K. E., Bourdier, J. L., & Bronto, S.: Origin, characteristics, and behaviour of lahars following the 1990 eruption of Kelud volcano, eastern Java (Indonesia). Bulletin of Volcanology, 59(7), 460-480, 1998.

Tierz, P., Woodhouse, M.J., Phillips, J.C., Sandri, L., Selva, J., Marzocchi, W., Odbert, H.M.: A Framework for Probabilistic Multi-Hazard Assessment of Rain-Triggered Lahars Using Bayesian Belief Networks 5, 1–23, doi:10.3389/feart.2017.00073, 2017.

Valentine, G. A., Palladino, D.M., Agosta, E., Teddeucci, J., Triglia, R.: Volcaniclastic aggradation in a semiarid environment, northwestern Vulcano Island, Italy. Geol. Soc. Amer. Bull. 110 (5), 630-643, 1998.

Vallance, J. W. and Iverson, R.M.: Lahars and their Deposits. The Encyclopedia of volcanoes. Academis, San Diego, 649-664, 2015.

Vallance, J. W., & Scott, K. M.: The Osceola Mudflow from Mount Rainier: Sedimentology and hazard implications of a huge clay-rich debris flow. Geological Society of America Bulletin, 109(2), 143-163, 1997.

Witham, C.S.: Volcanic disasters and incidents: a new database. J. Volcanol. Geotherm. Res. 148, 191-233, 2005.

Volentik, A.C.M., Connor, C.B., Connor, L.J., Bonadonna, C.: Aspects of volcanic hazard assessment for the Bataan nuclear power plant, Luzon Peninsula, Philippines. Volcan. Tecton. Hazard Assess. Nucl. Facil. 9780521887, 229–256, doi:10.1017/CBO9780511635380.010, 2009.

Yamakoshi T. and Suwa H.: Post eruption characteristics of surface runoff and sediment discharge on the slopes of pyroclastic-flow deposits, Mount Unzen, Japan. Transactions, Japanese Geomorphological Union, 21-4, p.469-497, 2000.

Yamamoto, H.: Erosion of the 1977–1978 tephra layers on a slope of Usu Volcano, Hokkaido. EOS, Transactions, American Geophysical Union, 5(2), 111-124, 1984.

Zanchetta, G., Sulpizio, R., Pareschi, M.T., Leoni, F.M., Santacroce, R.: Characteristics of May 5-6, 1998 volcaniclastic debris flows in the Sarno area (Campania, southern Italy): Relationships to structural damage and hazard zonation. J. Volcanol. Geotherm. Res. 133, 377–393. doi:10.1016/S0377-0273(03)00409-8, 2004.

Zanella, E., De Astis, G., Dellino, P., Lanza, R., & La Volpe, L.: Magnetic fabric and remanent magnetization of pyroclastic surge deposits from Vulcano (Aeolian Islands, Italy). Journal of volcanology and geothermal research, 93(3-4), 217-236, 1999.

Tables

Table 1: Hydraulic conductivity measured in the field

unit	test	*Ks* (m s^{-1})
Pal D	1	$6.8 \cdot 10^{-4}$
V 88-90	1	$6.0 \cdot 10^{-5}$
V 88-90	2	$7.5 \cdot 10^{-5}$

Table 2: Suction measured in the field on the 1888-90 tephra-fallout deposit and Mdϕ for Su5 and Su7 (Fig. 1). NA = Not available

Location	Suction (kPa)	Mdφ
Su1	25	NA
Su2	24	NA
Su3	27	NA
Su4	14	NA
Su5/V01	15	-0.27
Su6	15	NA
Su7/V08	20	0.90

Table 3: Summary of the physical characteristics of the tephra-fallout and lahar samples analysed. 30*: slope is measured on GIS (Geographic Information System). *Thick.* refers to the total deposit thickness. *Unit* refers to the 1888-1890 eruption (1888-90), the Palizzi D eruption (Pal D) and to the September 2017 lahars. *T* refers to the primary fallout and *L* to the associated lahars. For V1 and V2, the horizon shows the sampled section interval. *F1* and *F2* refers to the weight sample fraction < 1mm and < 63 µm, respectively.

Site	**Name**	**Thick. (cm)**	**Horizon**	**Unit**	**Slope (°)**	**Mdϕ**	**σϕ**	**F1**	**F2**
S La Fossa cone	V1A	100	0-6	1888-90 T	30	-0.37	1.80	35.13	3.23
	V1B	100	6-12	1888-90 T	30	0.08	1.46	39.99	2.60
	V1C	100	12-18	1888-90 T	30	-0.88	1.63	24.03	1.22
	V1D	100	18-24	1888-90 T	30	-0.41	1.68	32.81	0.84
	V1E	100	24-30	1888-90 T	30	-0.27	1.71	35.26	0.83
NW La Fossa cone base	V2A	50	0-6	1888-90 T	10	0.14	1.49	40.81	5.63
	V2B	50	6-12	1888-90 T	10	0.09	1.78	44.97	4.13
	V2C	50	12-18	1888-90 T	10	0.85	1.51	62.09	7.86
	V2D	50	18-24	1888-90 T	10	0.66	1.80	54.66	8.68
	V2E	50	24-30	1888-90 T	10	0.90	2.10	60.41	9.71
Pallizi valley	V3	25	-	Pal D T	10	-3.42	1.55	6.31	2.83
	V6	15	-	1888-90 L	5	2.07	1.78	84.12	12.38
S La Fossa cone	V5	15	-	1888-90 L	30	-0.12	1.83	37.46	5.73
Porto di Ponente	V7-1	26	-	1888-90 L	0-3	0.58	2.04	51.65	7.71
	V7-2	11	-	1888-90 L	0-3	0.90	1.75	58.91	7.87
	V7-3	10	-	1888-90 L	0-3	1.38	1.73	72.86	10.31
	V7-4	6	-	1888-90 L	0-3	1.29	1.76	68.65	8.92
NW La Fossa cone	V8	30	-	1888-90 L	30*	-0.29	1.67	33.27	2.51
	V9	40	-	1888-90 L	30	-0.27	1.69	34.04	3.29
	V10	30	-	1888-90 L	30	-0.24	1.68	34.02	2.85
	V11	20	-	2017 L	25*	-0.40	1.82	31.68	1.89
	V12	20	-	2017 L	25*	-0.02	1.82	39.42	3.16

Table 4: Geotechnical parameters for the subplinian tephra-fallout deposit (Pal D) and the Vulcanian tephra-fallout deposit associated with the 1888-90 eruption (Vulc).

unit	**K_s**	**Do ***	**φ´**	**Υ_s wet**	**Υ_s dry**	**c´**	**θ_s**	**θ_r**	**α**	**G_s**	**n**	**e**
	$m\ s^{-1}$	**$m^2\ s^{-1}$**	**deg**	**$kN\ m^{-3}$**	**$kN\ m^{-3}$**	**kPa**	**%**	**%**	**kPa^{-1}**	**-**	**-**	**-**
Pal D	$1 \cdot 10^{-2}$	$6.59 \cdot 10^{-3}$	54.00	13.70	6.64	0.00	0.72	0.04	0.93	2.42	0.72	2.57
Vulc	$8.50 \cdot 10^{-5}$	$3.28 \cdot 10^{-4}$	40.98	17.00	13.51	0.00	0.47	0.03	0.28	2.57	0.47	0.87

c': cohesion; **ϕ'**: friction angle; **γ_s**: total unit weight of the soil; **K_s**: saturated conductivity; **D_0**: saturated diffusivity; **θ_s**: saturated water content; **θ_r**: residual water content; **α:** Gardner parameter; **Gs**: specific gravity; **n:** porosity; **e**: void ratio. * Diffusivity was evaluated using the procedure proposed in the paper: Rossi et al. (2013).

Table 5: Input parameters for subplinian (*K_s* from literature), subplinian *(*K_s* measured in the field) and the 1888-90 Vulcanian eruption scenarios used for simulation with TRIGRS.

unit	**K_s ($m\ s^{-1}$)**	**D_o ($m^2\ s^{-1}$)**	**φ´ (deg)**	**Υ_s ($kN\ m^{-3}$)**	**c´ (kPa)**	**θ_s (%)**	**θ_r (%)**	**α (kPa^{-1})**
vulcanian	8.50x10-5	1 x 10-4	41.00	17.00	0.5	0.47	0.029	0.28
subplinian	$1x\ 10^{-2}$	$6.59x10^{-3}$	54.00	13.70	0.00	0.72	0.04	0.93
subplinian *	$6.8x10^{-4}$	$6.59x10^{-3}$	54.00	13.70	0.00	0.72	0.04	0.93

c': cohesion; **ϕ'**: friction angle; **γ_s**: total unit weight of the soil; **K_s**: saturated conductivity; **D_0**: saturated diffusivity; **θ_s**: saturated water content; **θ_r**: residual water content; **α:** Gardner parameter;

Table 6: Unstable areas (FS≤1) for long-lasting vulcanian eruption and subplinian (VEI: K_s from literature; VEI*: K_s measured in the field) calculated with TRIGRS for NW and S source areas (Fig. 7). Rainfall intensity 6.4 mm h^{-1} with a duration of 5 h. Thickness: tephra-fallout deposit thickness from probabilistic isopach maps considered in the model. Input parameters used for the simulation are described in table 5. VEI: Volcanic explosivity index.

Long-lasting Vulcanian eruption scenario

Probability (%)	Duration (month)	NW source area		S source area	
		Thickness (cm)	percentage of unstable area (%)	Thickness (cm)	percentage of unstable area (%)
25	9	11-14	34	13-17	57
25	12	14-18	69.5	16-22	81.6
25	18	21-26	89.4	24-31	66.6
25	24	26-33	52.3	30-39	22.9
75	9	6.5-8	0.08	7.6-10	0
75	12	8-10	7.1	8-12	10.9
75	18	9-12	17.9	11-14	31.1
75	24	10-12.8	20.7	11-15	36.8

Subplinian eruption scenario

Probability	VEI	NW source area		S source area	
		Thickness (cm)	percentage of unstable area (%)	Thickness (cm)	percentage of unstable area (%)
25	2	8-25	79.1	15-40	14.7
25	3	36-95	1.9	61-112	0.2
75	2	1-3	99.1	2-4	97.1
75	3	3-10	0.9	5-19	0.5
25	2*	8-25	99	15-40	97
25	3*	36-95	97	61-112	25
75	2*	1-3	99	2-4	97
75	3*	3-10	99	5-19	97

5

Table 7: Total and unstable volumes of primary tephra deposits for long-lasting vulcanian eruption and subplinian (VEI: K_s from literature; VEI*: K_s measured in the field) calculated with TRIGRS for NW and S upper catchments. NW and the S UP (upper catchments) have the same area (4665 m^2), with a mean slope of 43.5° and 40.1°, respectively. Rainfall intensity 6.4 mm h^{-1} with a duration of 5 h. Thickness: tephra-fallout deposit thickness from probabilistic isopach maps considered in the model.

Long-lasting Vulcanian eruption scenario

Probability (%)	**Duration (months)**	**NW catchment**			**S catchment**		
		Thickness (cm)	**Volumes (m^3)**		**Thickness (cm)**	**Volumes (m^3)**	
			Total	**Unstable**		**Total**	**Unstable**
25	9	11-13	574	246	15-16	734	585
25	12	14-16	748	601	20-21	959	952
25	18	20-24	1061	991	28-30	1353	1105
25	24	25-30	1326	861	35-37	1689	95
75	9	6.5-7.5	333	0	9	427	0
75	12	9-10	417	0	11	533	21
75	18	9.5-11.5	489	47	13-14	627	231
75	24	10-12	507	74	13.5-14.5	649	319

Plinian eruption scenario

Probability (%)	**VEI**	**NW catchment**			**S catchment**		
		Thickness (cm)	**Volumes (m^3)**		**Thickness (cm)**	**Volumes (m^3)**	
			Total	**Unstable**		**Total**	**Unstable**
25	2	11-15	589	563	32-40	1663	0
25	3	37-58	2455	0	101-112	5112	0
75	2	1.2-2	77	77	3.2-3.6	187	185
75	3	2-8	245	244	13-16	736	401
25	2*	11-15	589	604	32-40	1663	1636
25	3*	37-58	2455	2455	101-112	5112	0
75	2*	1.2-2	77	77	3.2-3.6	187	187
75	3*	2-8	245	245	13-16	736	731

Table 8: Measured median grain size, hydraulic conductivity and infiltration capacity on tephra-fallout (TF) and PDC deposits near volcanic vents

Eruption	Deposit type	Median grain size, Mdφ	Annual precipitation (mm)	Hydraulic conductivity (m/s)	Post-eruption infiltration capacity (m/s)	Data source
Vulcano (1888-90 Vulcanian)	TF	-0.90 - 1	500	8.5x10^{-5}	ND	this study
Vulcano (Pal D subplinian)	TF	-3.42	500	1x10^{-2}	ND	this study
Cordón Caulle 2011	TF-ash (unit III)	2.15	2500-3000	5x10^{-5}	ND	a
Cordón Caulle 2011	TF-lapilli (unit I-II)	-1.5	2500-3000	3.9x10^{-2}	ND	a
Chaitén 2008	TF	< 3	2600-4300	ND	ND	b
Mt Pinatubo 1990	PDC	0-3		ND	1x10^{-4}	c
	TF	-1.1- 1.7	1950	ND	ND	c
Mt Unzen 1990-95	PDC	-1-1	3100	ND	1.25x10^{-5} 5x10^{-6}	d
Mt St Helen 1980	TF	1.73	1200	ND	1.9x10^{-6} 1.13x10^{-6}	e

ND = No data. References: a) Baumann et al., 2018 b) Pierson et al., 2013 c) Daag, 2003 d) Yamakoshi and Suwa, 2000 e) Leavesley et al., 1989.

Figures

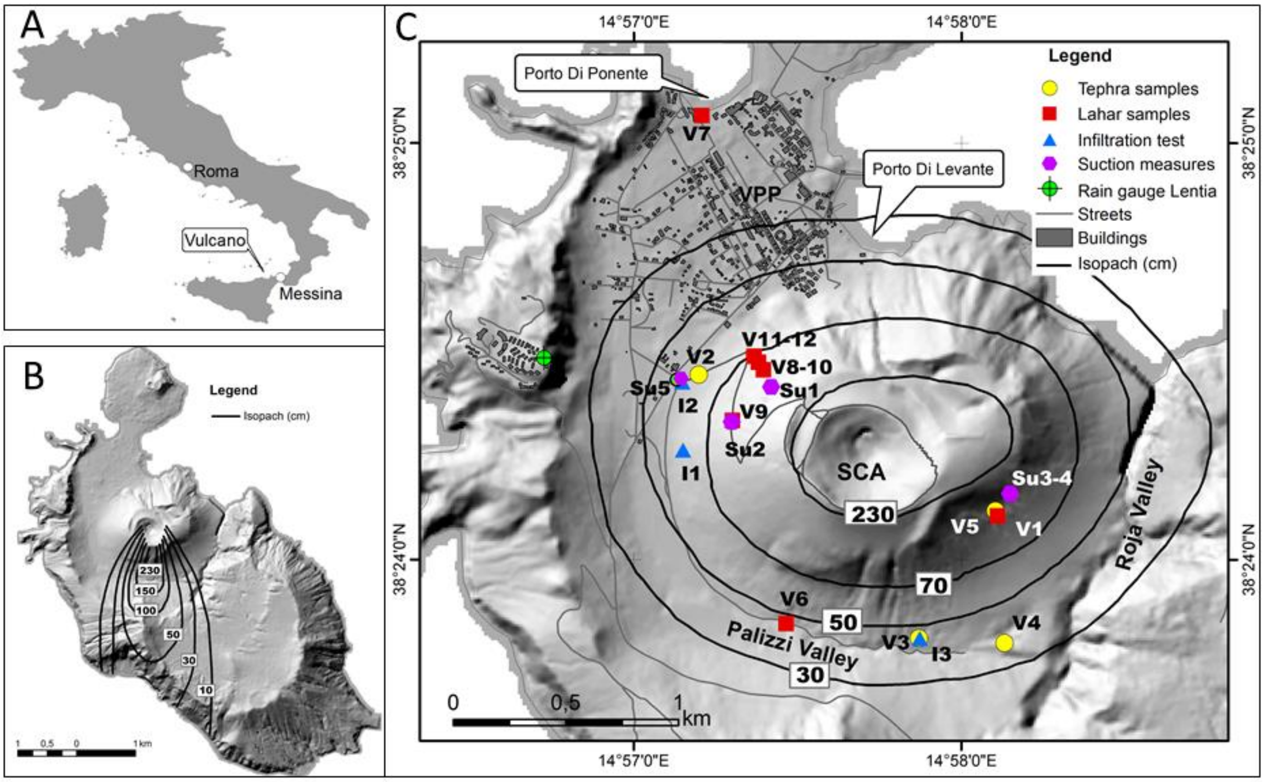

Figure 1: Overview of the study area. A) location of the island of Vulcano in Italy; B) Isopach map on shaded relief of Vulcano Island of the cumulative tephra-fallout Pal D deposit (after Di Traglia (2011); C) isopach map of the cumulative 1888-90 tephra-fallout deposit (after Di Traglia, 2011) and sample locations. Sample names refer to *V* samples of tephra fallout (yellow circles) and lahars (red squares), *I* infiltration measures (blue triangle) and *Su* suction measurements (pink diamond). *SCA*: summit cone area. *VPP*: Vulcano Porto Plain. The rain gauge of Lentia is also shown (green circle).

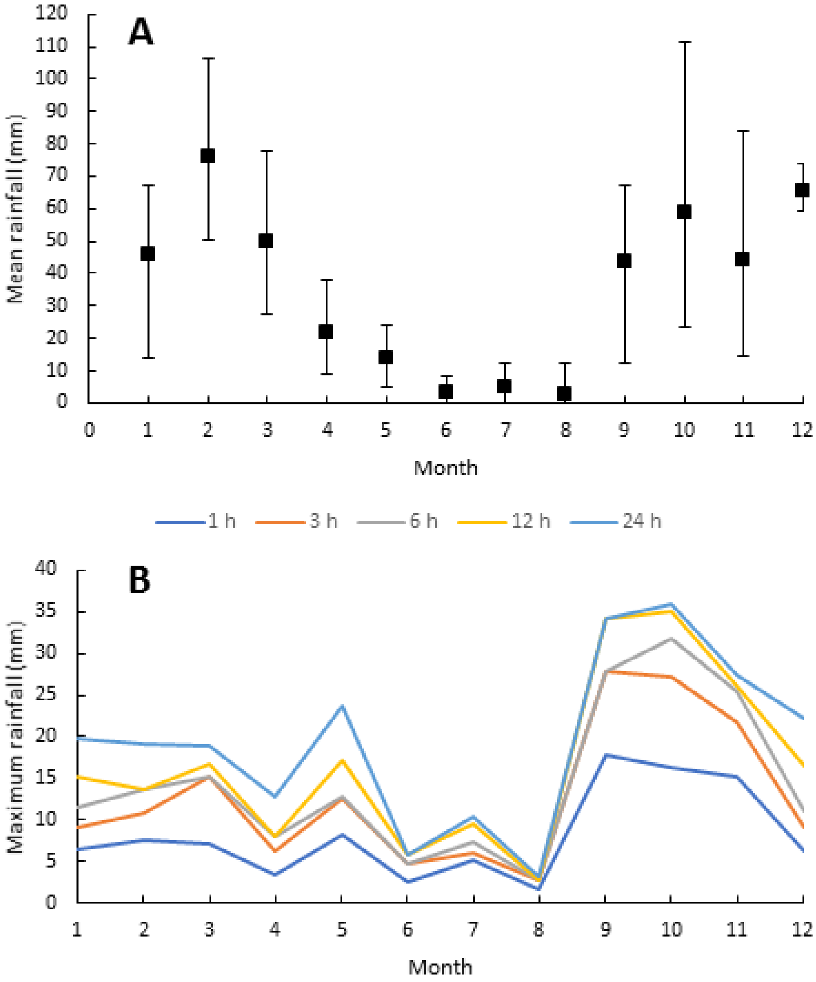

Figure 2: A) Mean monthly rainfall (mm) observed at Lentia station (Fig. 1) between 2010 and 2014 (error bars also indicate minimum and maximum values); B) Maximum monthly rainfall within 3, 6, 12 and 24 hours (data from INGV Palermo).

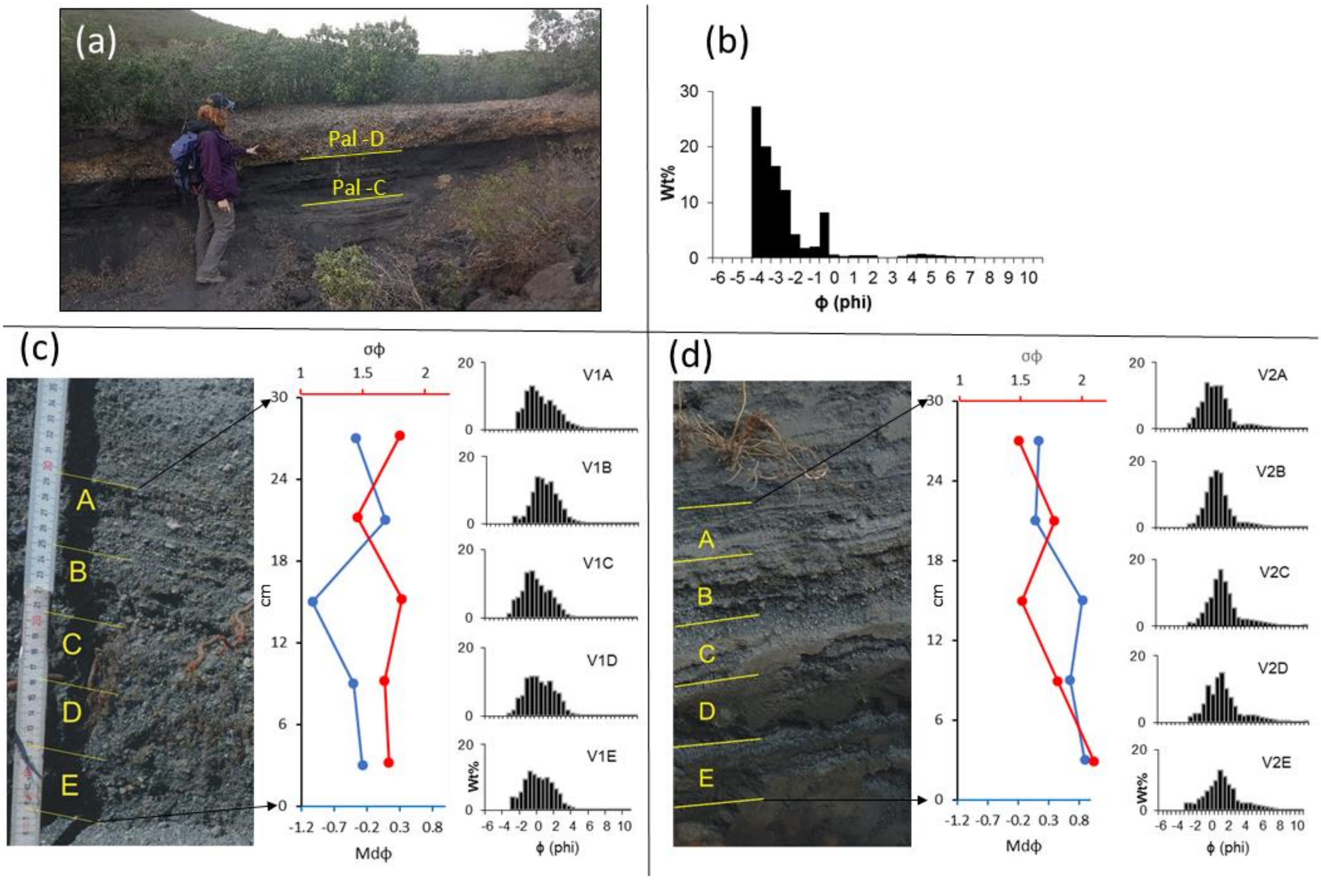

Figure 3: A) Pal D subplinian tephra fallout deposit outcrop (V3, Fig.1) B) grainsize distribution Pal D subplinian tephra fallout deposit; C) and D) Mdφ, σφ and grainsize distribution of the first 30 cm of the tephra-fallout deposit associated with the 1888-90 Vulcanian eruption for stratigraphic sections V1 and V2 (Fig. 1) (thickness of layers analysed: A (24-30 cm); B (24-18 cm); C (18-12 cm); D (12-6cm); E (6-0 cm).

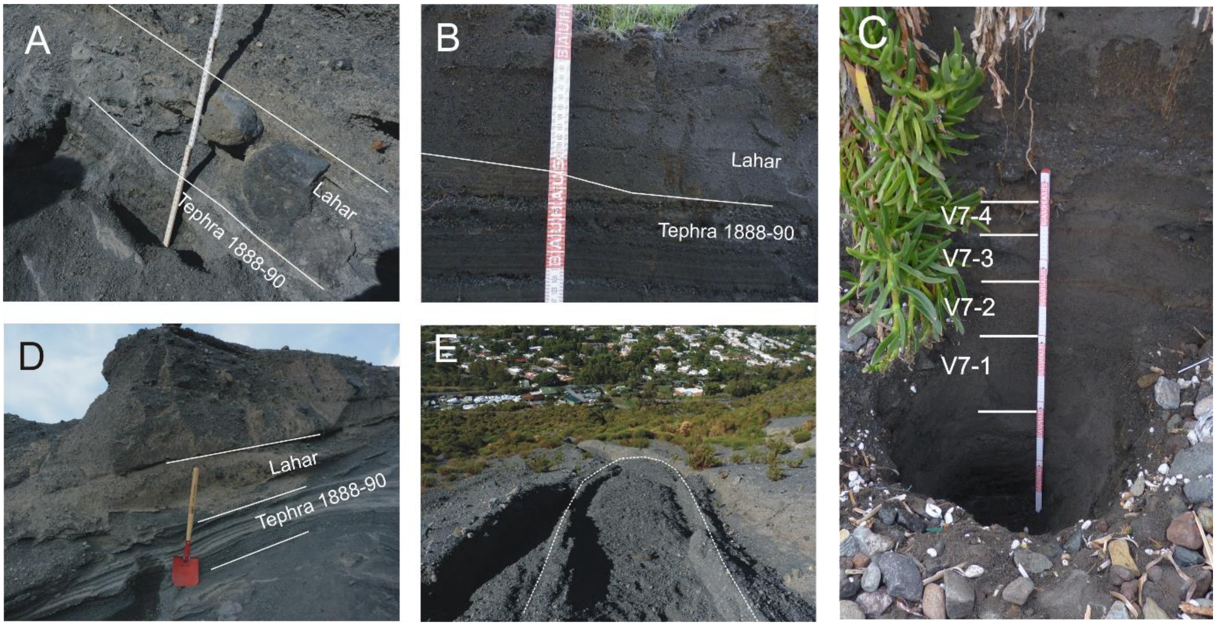

Figure 4: A) Lahar levee deposit (sample V5 in Fig. 1) above the 1888-90 tephra-fallout, located in a channel cut on the S of La Fossa cone. B) Lahar deposit (sample V6) above the 1888-90 tephra-fallout in the Palizzi valley. C) Profile observed at the beach side in Porto di Ponente (1) is a 14 cm bed of coarse ash, with a 1cm thick grey fine ash grey layer, this is the primary 1888-90 AD tephra-fallout; Layer V7-1 is a 26 cm lahar deposit of coarse ash to fine lapilli inversely graded; Layer V7-2 is a 11 cm fine lapilli lahar deposit with a 1 cm soil on the top; V7-3 is a 10 cm lahar deposit of coarse to fine ash with a soil on the top and 6 cm lahar deposit (V7-4) of coarse to fine ash with the recent soil on the top. D) Several lahar deposits located in a channel on the NW of La Fossa cone: the first deposit above 1888-90 was sampled (V9 in Fig. 1). E) September 2017 lahar deposit confined within the channel; the white lines mark the contour of the deposit.

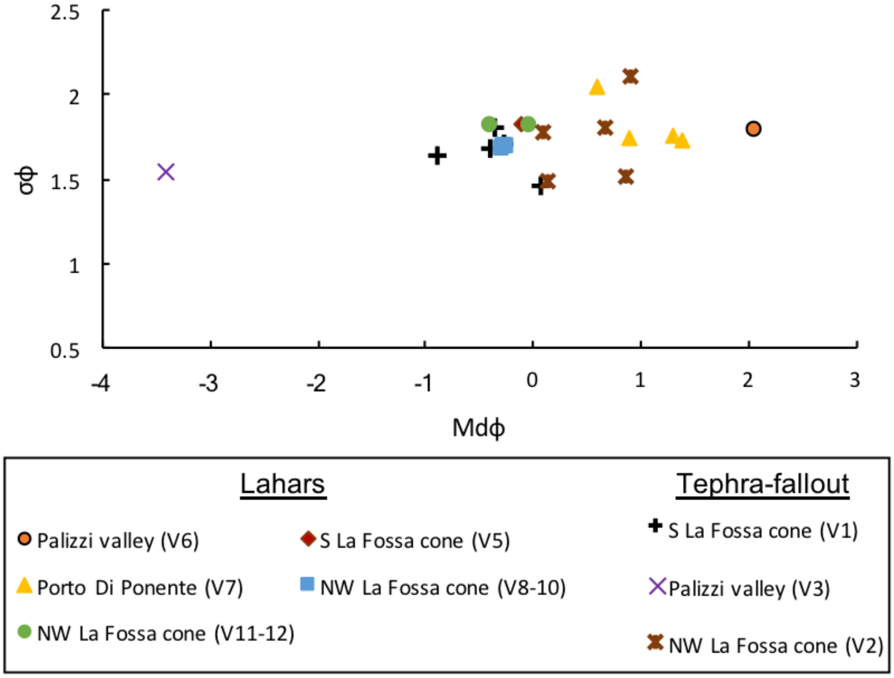

Figure 5: Mdφ vs σφ diagram for the lahar matrix and tephra-fallout deposits. Porto Di Ponente (orange triangle) correspond to samples: V7-1, V7-2,V7-3, V7-4 S (Fig 4C); La Fossa cone V1 (black cross): V1A, V1B,V1C, V1D, V1E (Fig. 3C). NW La Fossa cone V2 (brown star): V2A, V2B, V2C, V2D, V2E (Fig. 3D).

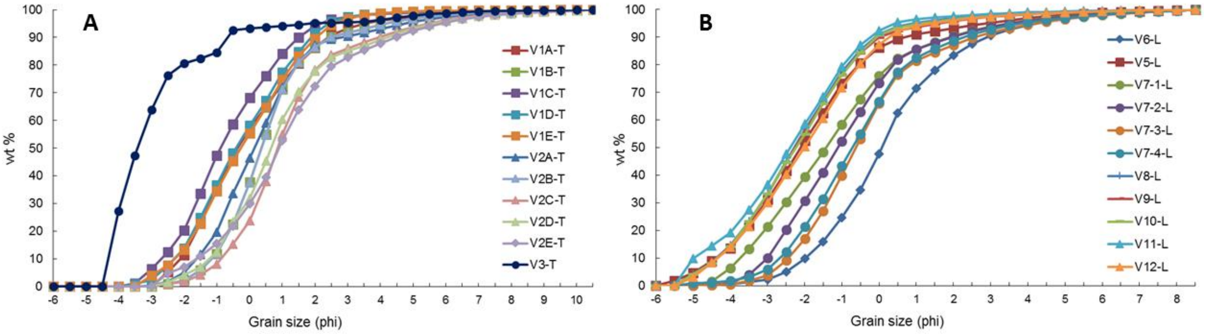

Figure 6: Grainsize distribution for A) primary and B) remobilized deposits (lahars). See Table 3 for a reference of sample numbers.

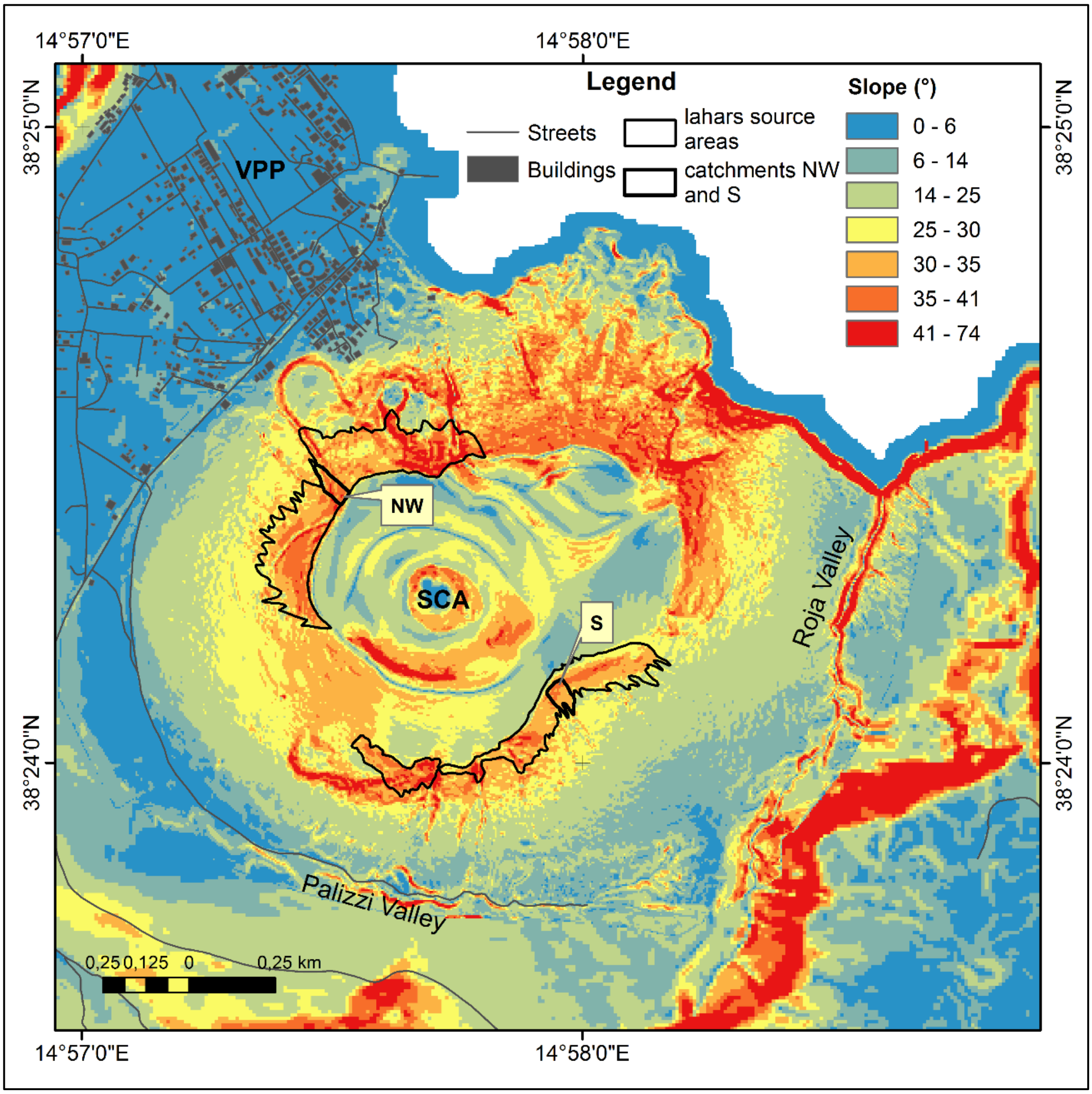

5 **Figure 7: Slope map for the La Fossa cone and surrounding areas. North West and South lahar source areas are indicated with a black contour. The NW and S upper catchment are indicated with a black contour. *SCA*: summit cone area; *VPP*: Vulcano Porto Plain**

10

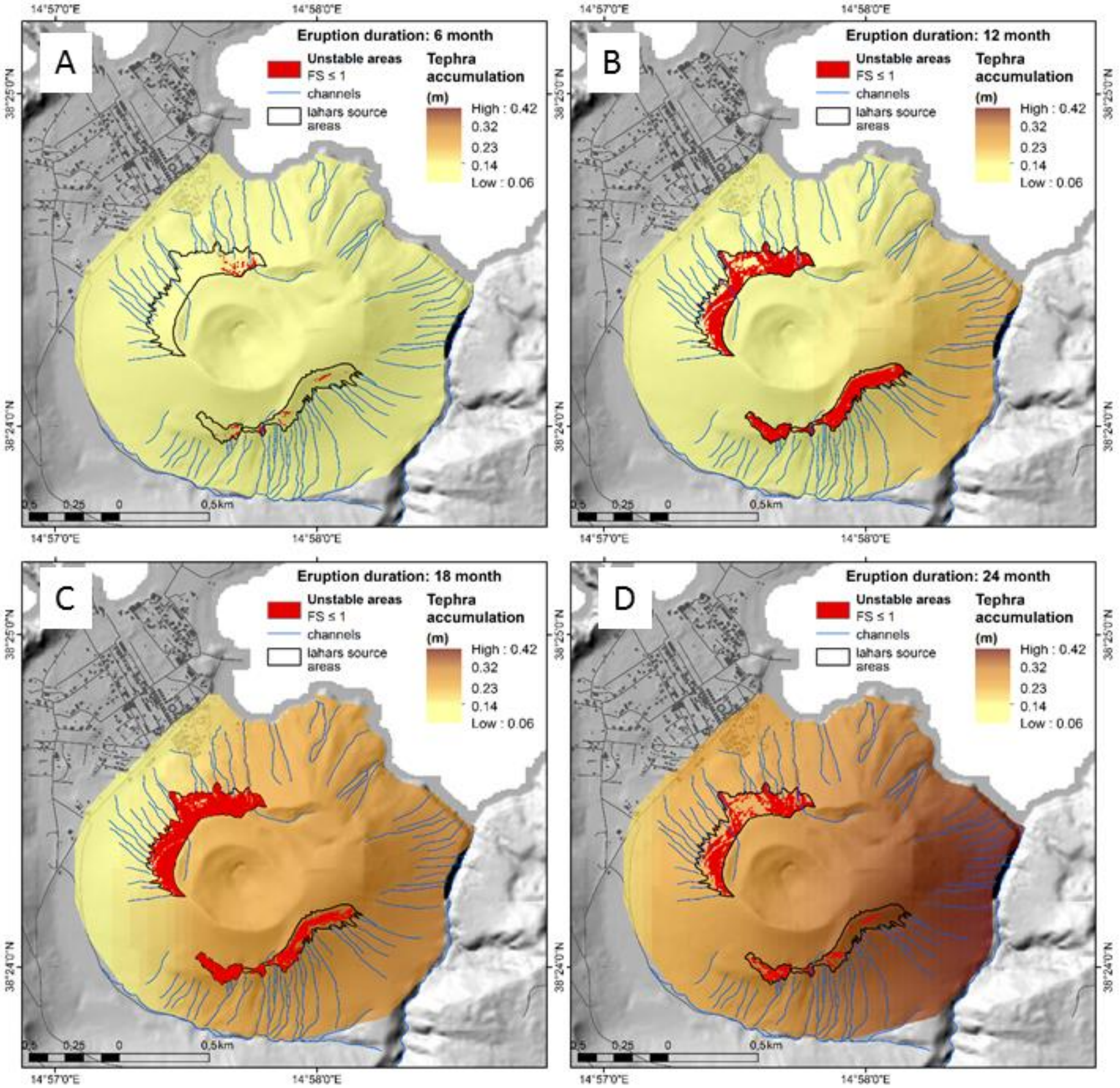

Figure 8: Probabilistic isopach maps (converted from the probabilistic isomass maps of Biass et al. (2016) based on deposit density) and corresponding instability maps compiled with TRIGRS for a Vulcanian eruption with: A) an eruption duration of 6 months and a probability of occurrence of 25%; B) an eruption duration of 12 months and a probability of occurrence of 25%; C)) an eruption duration of 18 months and a probability of occurrence of 25%. D) an eruption duration of 24 months and a probability of occurrence of 25%. The rainfall intensity is 6.4 mm h^{-1} with a duration of 5h for all the scenarios and the parameters for the 1888-90 Vulcanian deposits are listed in table 5.

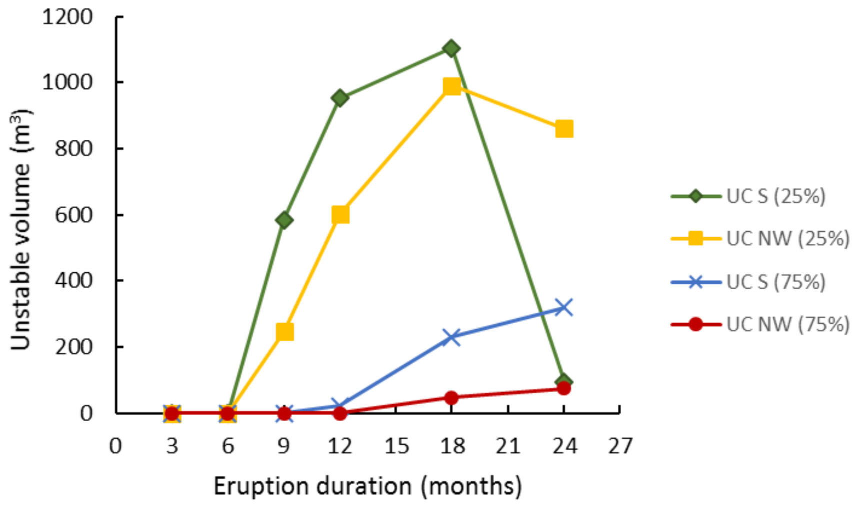

Figure 9: Unstable tephra-fallout volume for the S and NW upper catchments obtained with TRIGRS for eruption durations of 3, 6, 9, 12, 18 and 24 and for probabilities of occurrence of 25% and 75%. UC: upper catchment (see Fig. 7b).

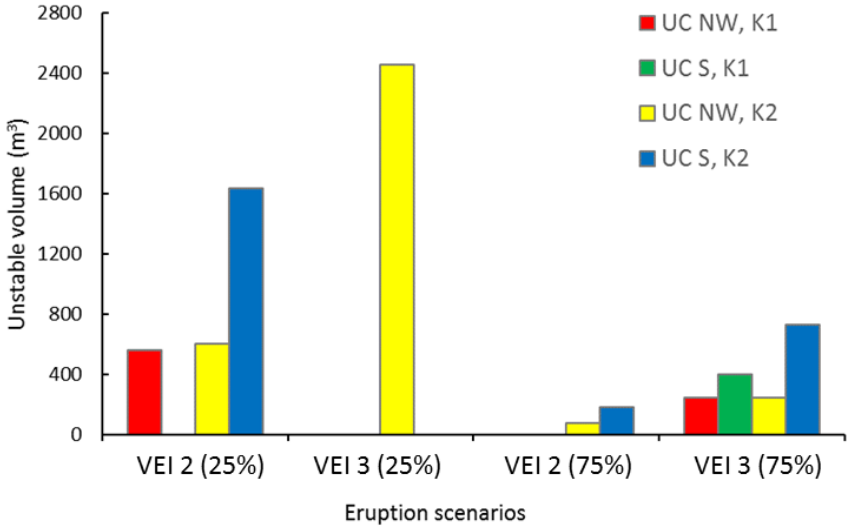

Figure 10: Unstable tephra-fallout volume for the S and NW upper catchments obtained with TRIGRS for: 1) the subplinian scenarios VEI2 and VEI3 with a K_s = 1x10^{-2} m s^{-1} (from literature) and VEI2, VEI3 with a K_s= 6.8x10^{-4} m s^{-1} (as measured in the field) and the probabilities of occurrence 25% and 75%.

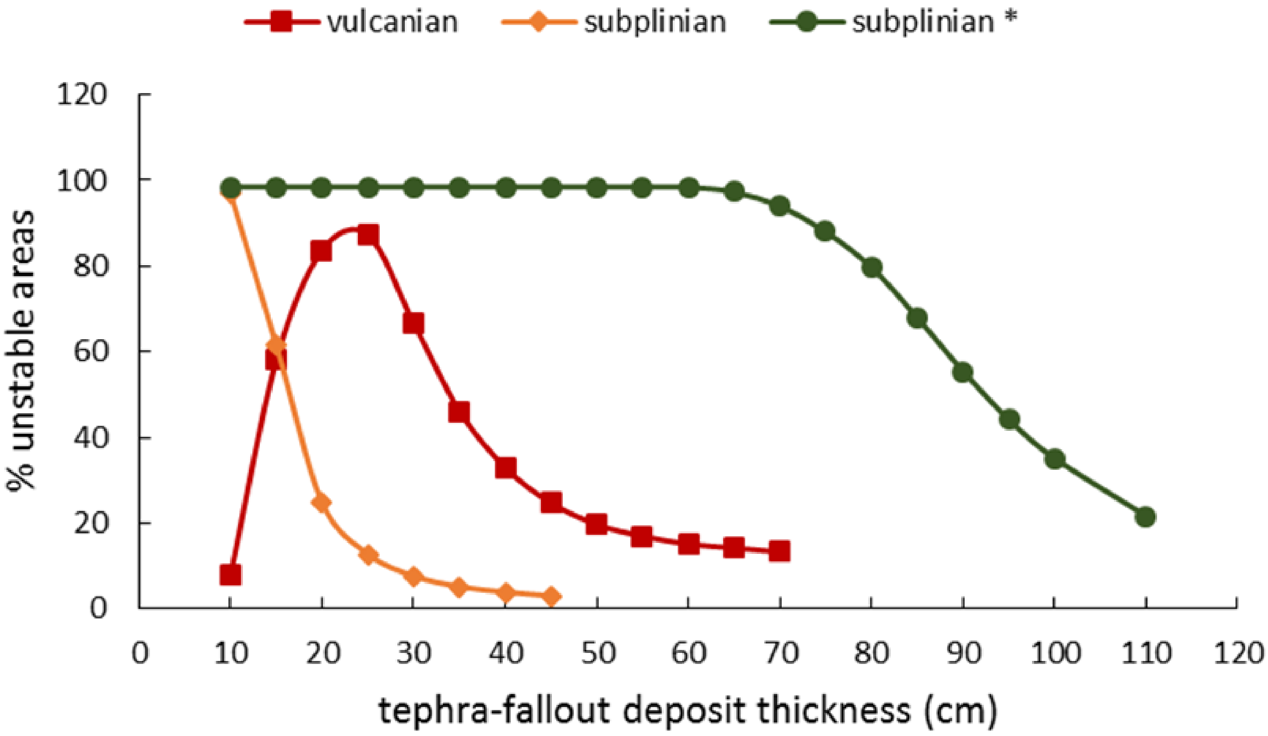

Figure 11: Percentage of unstable area for the NW and S lahar source areas simulated with TRIGRS for tephra-fallout deposit thicknesses between 0.1-1.1 m and a rainfall intensity of 6.4 mm h^{-1} with a duration of 5 hours and parameters for: Vulcanian tephra-fallout deposits (red squares); subplinian tephra-fallout deposits with K_s = 1x10^{-2} m s^{-1} (value from literature; orange diamonds) and subplinian tephra-fallout deposits with K_s= 6.8x10^{-4} m s^{-1} (value measured in the field; green circles).

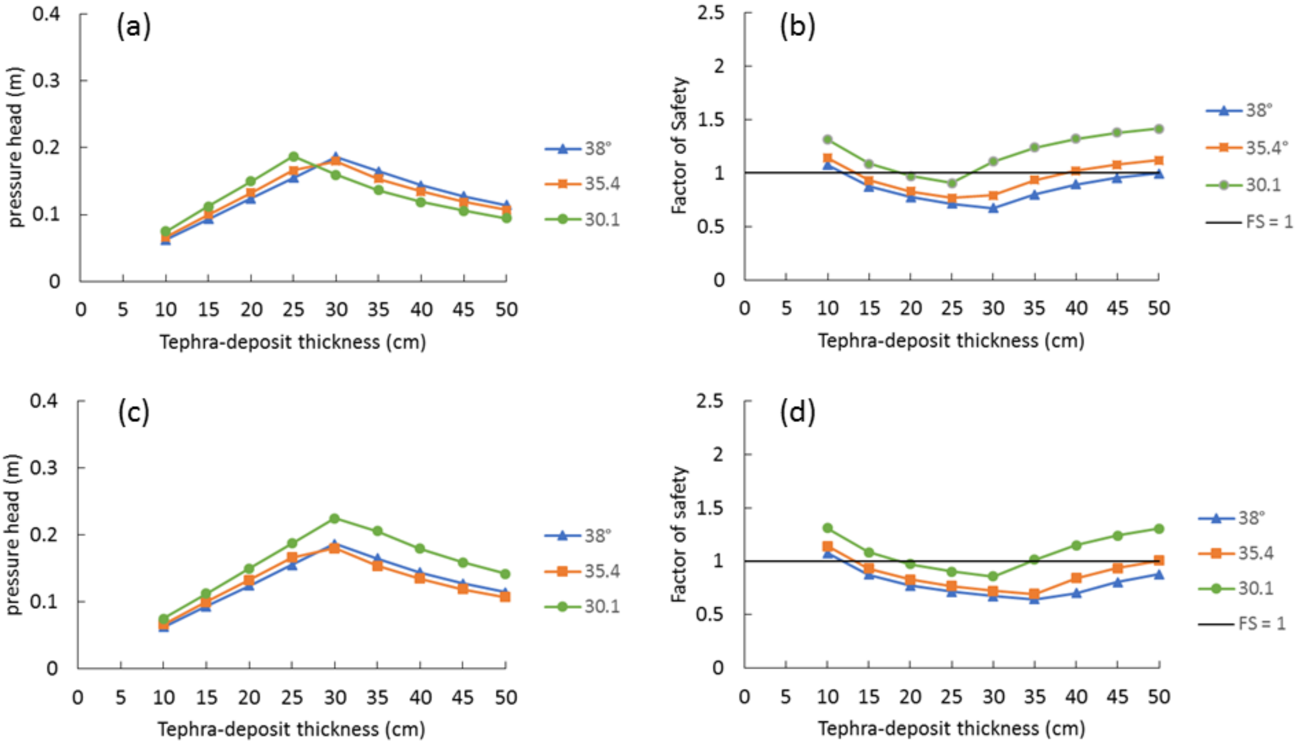

Figure 12: Total pressure head and factor of safety for tephra versus tephra-fallout deposit thicknesses between 0.1 and 0.55 m for Vulcanian tephra-fallout deposits (table 5) and a rainfall intensity of: A) and B) 6.4 mm h^{-1} with a duration of 5 hours (I/K_s = 0.02); C) and D) 15.5 mm h^{-1} with a duration of 3 hours (I/K_s = 0.05)

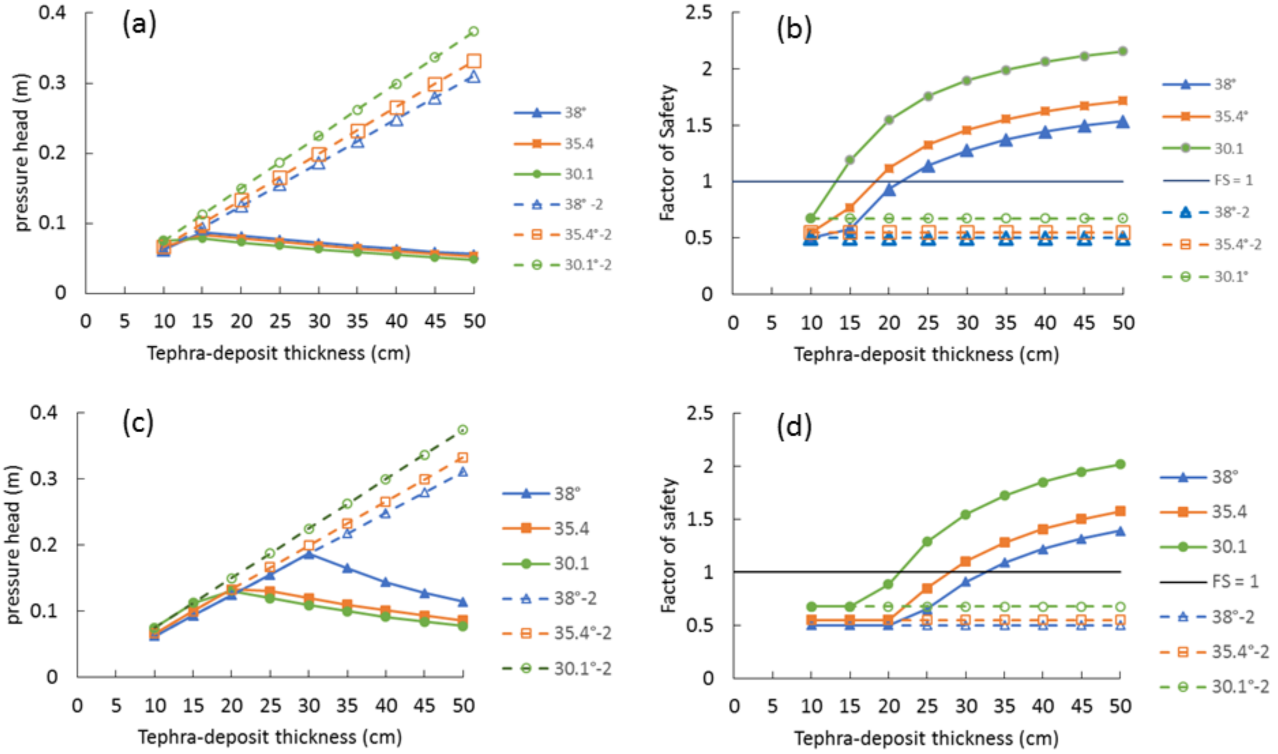

Figure 13: Total pressure head and factor of safety for tephra versus tephra-fallout deposit thicknesses between 0.1 and 0.55 m for subplinian tephra-fallout deposits with K_s = 1x10^{-2} m s^{-1} and K_s= 6.8x10^{-4} m s^{-1} (dashed lines) for two different rainfall intensities and durations: A and B) 6.4 mm h^{-1} with a duration of 5 hours. C) and D) 15.5 mm h^{-1} with a duration of 3 hours.